Multiple branches of travelling waves for the Gross-Pitaevskii equation

David Chiron, Claire Scheid

MULTIPLE BRANCHES OF TRAVELLING WAVES FOR THE GROSS-PITAEVSKII EQUATION

David Chiron[1] and Claire Scheid[2]

Abstract. Explicit solitary waves are known to exist for the Kadomtsev-Petviashvili-I (KP-I) equation in dimension 2. We first address numerically the question of their Morse index. The results confirm that the lump solitary wave has Morse index one and that the other explicit solutions correspond to excited states. We then turn to the 2D Gross-Pitaevskii (GP) equation which in some long wave regime converges to the (KP-I) equation. Numerical simulations already showed that a branch of travelling waves of (GP) converges to a ground state of (KP-I), expected to be the lump. In this work, we perform numerical simulations showing that other explicit solitary waves solutions to the (KP-I) equation give rise to new branches of travelling waves of (GP) corresponding to excited states.

1991 Mathematics Subject Classification. 35B38, 35C07, 35J61, 35Q40, 35Q55.

January 23, 2018.

1. Motivations

1.1. (NLS) with nonzero condition at infinity

The nonlinear Schrödinger equation (NLS) with nonzero condition at infinity appears in a variety of physical problems: condensed matter physics (see [34]), Bose-Einstein condensates and superfluidity (*cf.* [37], [1]), as well as nonlinear Optics (see [26]). Depending on the physical problem, several nonlinearities may be of interest (see the examples and references quoted in [12, 15]). The most popular one is of cubic type and leads to the well-known Gross Pitaevskii (GP) equation for which NLS equation writes:

$$i\frac{\partial \Psi}{\partial t} + \Delta \Psi = \Psi(|\Psi|^2 - 1). \tag{GP}$$

In this work, we shall consider the GP equation in space dimension two and with the following condition at infinity: $|\Psi| \to 1$ as $|x| \to +\infty$. The GP equation is the Schrödinger flow associated with the Ginzburg-Landau energy

$$E(u) = \int_{\mathbb{R}^2} |\nabla u|^2 + \frac{1}{2}\int_{\mathbb{R}^2} (|u|^2 - 1)^2.$$

Keywords and phrases: Non Linear Schrödinger equation, travelling waves, Kadomtsev-Petviashvili equation, vortex

[1] Université Côte d'Azur, CNRS, LJAD, France, chiron@unice.fr

[2] Université Côte d'Azur, Inria, CNRS, LJAD, France, Claire.Scheid@unice.fr

For a nowhere vanishing solution, GP can be recast into a hydrodynamical form, via the Madelung transform $\Psi = \sqrt{\rho}e^{i\varphi}$:

$$\begin{cases} \partial_t \rho + 2\nabla \cdot (\rho \nabla \varphi) = 0 \\ \\ \partial_t \varphi + |\nabla \varphi|^2 + \rho - 1 = \dfrac{\Delta \sqrt{\rho}}{\sqrt{\rho}}. \end{cases} \tag{1}$$

This is an incompressible irrotational Euler type system with an additional term called quantum pressure in the right-hand side of the second, Bernoulli type, equation. Neglecting the quantum pressure and linearizing around the constant state $(\rho = 1, \varphi = 0)$ corresponding to the condition at infinity, one obtains the free wave equation:

$$\begin{cases} \partial_t a + \nabla \cdot V = 0 \\ \\ \partial_t V + 2\nabla a = 0 \end{cases}$$

with $(a, V) = (\sqrt{\rho} - 1, \nabla\varphi)$. This allows for the definition of the speed of sound $\mathfrak{c}_s = \sqrt{2}$ (see [1,34] for details).

In this work, we furthermore focus on the travelling waves solutions. We consider the ansatz $\Psi(t, (x_1, x_2)) = u(x_1 - ct, x_2)$, with $(t, x_1, x_2) \in \mathbb{R}^3$, that is representing a wave travelling in the direction x_1 with speed c. The profile u of the travelling wave then solves:

$$ic\partial_{x_1} u - \Delta u + u(|u|^2 - 1) = 0. \tag{TW$_c$}$$

The condition at infinity is now $u \to 1$, up to a phase change. Indeed, it was conjectured in [25] that u tends to 1 at some algebraic rate, and this has been proved (if u has finite energy) in [23].

In addition to E, the momentum is also a conserved quantity, reflecting the invariance by space translation of GP, that is also central to illustrate the qualitative behavior of the travelling waves solutions. For u tending suitably to 1 at infinity, its first component reads

$$P(u) = \int_{\mathbb{R}^2} \langle i(u-1), \partial_{x_1} u \rangle,$$

with $\langle \cdot, \cdot \rangle$ the real scalar product on $\mathbb{C}$ (the second component $\int_{\mathbb{R}^2} \langle i(u-1), \partial_{x_2} u \rangle$ is also conserved but will be useless for the travelling waves propagating in the x_1 direction). The study of the behavior of the variations of the energy E and the momentum P as the speed c varies is at the heart of the understanding of (among others) the stability properties of the travelling wave solutions. Thus the Energy *vs* Momentum diagram given as a speed parametrized curve is especially instructive. We refer to the pioneering work of C.A. Jones, P.H. Roberts in two space dimensions and tridimensional axisymmetric for GP in [25] and to the more recent works of [12,15] for more general non linearities. In all these studies, the computed solutions are critical points of the action $\mathcal{F}_c = E - cP$ that are characterized as minimizers of some functional under a single constraint (for instance, in [25], the energy is minimized at fixed momentum). Therefore a Morse index equal to one is expected, i.e. the Hessian of $\mathcal{F}_c$ has only one negative eigenvalue. We recall in figure 1 the diagram for the case of 2D travelling waves of GP (issued from [25]), and we shall call this branch the JR branch. Several mathematical results are known about this JR branch: see [9], [6], [30] (in dimension larger than two) and [14].

In this paper, on the contrary to the previous mentioned references, we propose to numerically investigate the possible existence of solutions to (TW$_c$), which may be of Morse index > 1; that is excited states. We give a positive answer to this question. As a matter of fact, we obtain that there exists at least 4 new branches of travelling wave solutions in the Energy-Momentum diagram as depicted in figure 2 and in the Momentum-Speed diagram in figure 3 (the blue branch corresponds to the blue one in figure 1 and is the JR branch). The variation of P (or E) with respect to c is related to the concavity/convexity of the function $P \mapsto E$ (along the curve), in view of the Hamilton group relation

$$c = \frac{dE}{dP} \qquad \text{or} \qquad \frac{dE}{dc} = c\frac{dP}{dc}$$

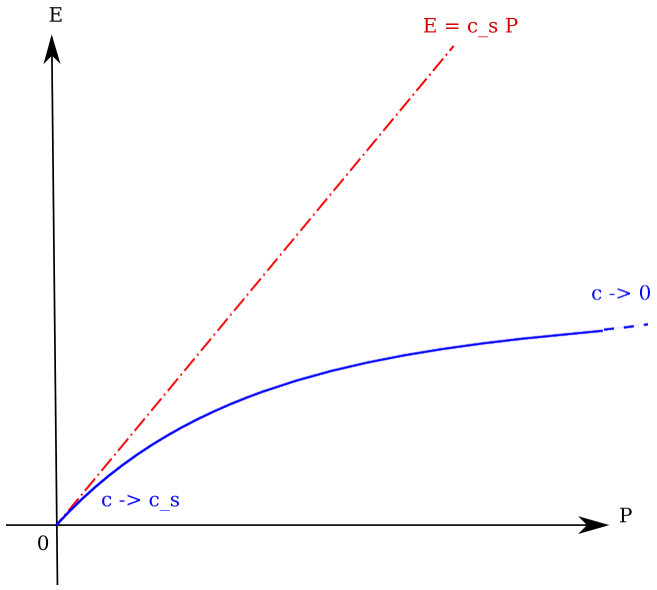

FIGURE 1. Energy-Momentum diagram for 2D travelling waves of GP: the Jones-Roberts branch

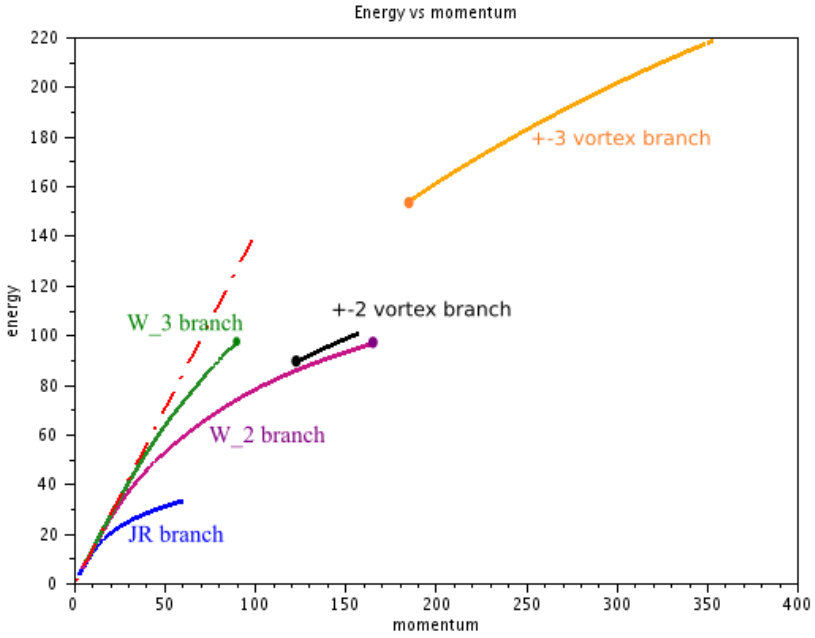

FIGURE 2. Energy-Momentum diagram with the multiple branches of 2D travelling waves of GP

along the curve (see [25]). It is highly plausible that there exist many other ones. To construct these new branches, we strongly rely on the knowledge of the asymptotics $c \to 0$ and $c \to \mathfrak{c}_s$.

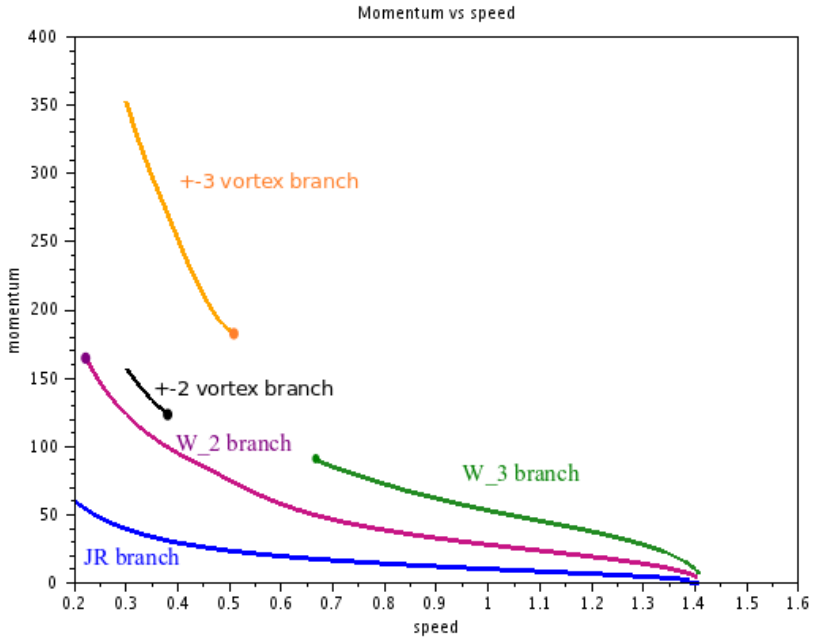

FIGURE 3. Momentum-Speed diagram with the multiple branches of 2D travelling waves of GP

1.2. **Vortex asymptotics** $c \approx 0$**.**

A vortex is a particular stationary solution of the GP equation, see [21]. In polar coordinates it writes

$$V_n(x) = \mathfrak{a}_n(r)e^{in\theta}, \tag{2}$$

with n a given nonzero integer called the *degree* of the vortex. The modulus $\mathfrak{a}_n$ solves the ODE

$$\mathfrak{a}_n'' + \frac{\mathfrak{a}_n'}{r} - \frac{n^2}{r^2}\mathfrak{a}_n + \mathfrak{a}_n(1 - \mathfrak{a}_n^2) = 0, \tag{3}$$

with $\mathfrak{a}_n(0) = 0$ and $\lim_{r\to+\infty} \mathfrak{a}_n(r) = 1$. We refer to [41], [24], [10] for the analysis of (3).

Quite often, we call vortex any zero of the wave function, and it is expected that the wave function is close to some V_n near this zero. The vortex solution V_n is of infinite energy. However configurations involving several vortices (with possibly different degrees) could lead to finite energy solutions. At small speeds $c \to 0$, the travelling waves of the JR branch for the GP equation exhibit two vortices: the first one is of degree $+1$ and is located at z_1 and the second one is of degree -1 and is located at z_2, with $z_1 = -z_2 \approx (0, 1)/c$, see figure 4 for a plot. A good approximation of this travelling wave is then given by

$$u_c(x) \approx V_1(x_1, x_2 - 1/c)V_{-1}(x_1, x_2 + 1/c). \tag{4}$$

The paper [9] provides a rigorous mathematical justification for the asymptotic limit $c \approx 0$ for the travelling waves of the JR branch.

Since the vortices are well separated when $c \to 0$, an asymptotic description by the Kirchhoff energy, very similar to what is known for classical incompressible fluids (see [27]), is possible. More precisely, assume that u

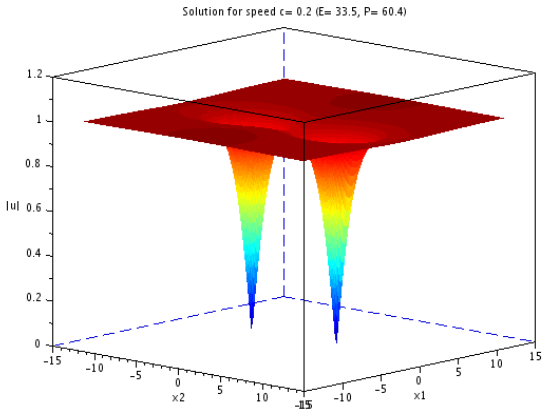

FIGURE 4. Travelling wave of the JR branch for $c = 0.2$ with two $(+1, -1)$ vortices

is a wave function involving p vortices ($p \geqslant 2$), each one located at z_k and of degree n_k, in the sense that

$$u(x) \approx \prod_{k=1}^{p} V_{n_k}(x - z_k). \tag{5}$$

We assume that the vortices are well separated, that is $z_k = Z_k/c = c^{-1}(Z_{k,1}, Z_{k,2}) \in \mathbb{R}^2$, with the Z_k's such that, as $c \to 0$, $|Z_k|$ are of order one and $|Z_k - Z_j|$ does not go to 0. We also assume that $\sum_{k=1}^{p} n_k = 0$, in order to have finite energy. Then, [31] (see also [7]) shows the following asymptotic expansion

$$E(u) = 2\pi|\ln c| \sum_{k=1}^{p} n_k^2 + \sum_{k=1}^{p} \gamma(|n_k|) + \mathscr{E}(Z, \mathsf{n}) + o_{c\to 0}(1),$$

where $\gamma(|n|)$ is the core energy of the vortex of degree n, $\mathsf{n} = (n_1, \ldots, n_p) \in \mathbb{Z}^p$ and where

$$\mathscr{E}(Z, \mathsf{n}) \stackrel{\text{def}}{=} -2\pi \sum_{j \neq k} n_j n_k \ln |Z_j - Z_k|$$

is the Kirchhoff interaction energy. The point vortex system obtained for the Euler incompressible equations, which is the Hamiltonian flow associated the Kirchhoff energy $\mathscr{E}$, may actually be derived for GP, see *e.g.*, [19], [31] and [7] for rigorous results.

For a wave function u with such well separated vortices, the asymptotic for the momentum has been given in [9]:

$$P(u) \approx \frac{2\pi}{c} \sum_{k=1}^{p} n_k Z_{k,2}.$$

As a consequence, the corresponding action for u is given by

$$E(u) - cP(u) = 2\pi|\ln c| \sum_{k=1}^{p} n_k^2 + \sum_{k=1}^{p} \gamma(|n_k|) + \mathscr{F}(Z, \mathsf{n}) + o_{c\to 0}(1),$$

where

$$\mathscr{F}(Z,\mathsf{n}) \stackrel{\text{def}}{=} -2\pi \sum_{j\neq k} n_j n_k \ln|Z_j - Z_k| - 2\pi \sum_{k=1}^{p} n_k Z_{k,2}.$$

Since the first two terms in the expansion of the action do not depend on the positions Z of the vortices, it is natural to think that if u is a travelling wave for GP with vortices as in (5), then $(Z_1,\dots,Z_p)$ is a critical point of the reduced action $\mathscr{F}$, that is a solution to the nonlinear system

$$\forall k \in [\![1,p]\!], \qquad 2 \sum_{\substack{1\leqslant j\leqslant p \\ j\neq k}} n_j \frac{Z_j - Z_k}{|Z_j - Z_k|^2} = \begin{pmatrix} 0 \\ 1 \end{pmatrix}. \tag{6}$$

The proof that (6) is necessary may be found in [4] for the Ginzburg-Landau model (in a bounded domain and a Dirichlet boundary condition). If the travelling wave has two $(+1,-1)$ vortices (then $p=2$) and $n_1 = 1$, $n_2 = -1$, we may without loss of generality freeze the translation invariance by assuming $Z_1 + Z_2 = 0$, and the equation (6) then reduces to

$$\frac{Z_1}{|Z_1|^2} = \begin{pmatrix} 0 \\ 1 \end{pmatrix},$$

and the solution is $Z_1 = (0,1)$, which is the location of the vortices for the JR branch.

1.3. **Transonic limit $c \approx \mathfrak{c}_s$**

As $c \to \mathfrak{c}_s$, the travelling waves are expected to behave as rarefaction waves driven by the Kadomtsev-Petviashvili I (KP-I) equation. Following [25], [26], we introduce the following scalings:

$$\varepsilon = \sqrt{\mathfrak{c}_s^2 - c^2}, \quad z_1 \stackrel{\text{def}}{=} \varepsilon x_1, \quad z_2 \stackrel{\text{def}}{=} \varepsilon^2 x_2, \tag{7}$$

and the ansatz

$$u(x) = \Big(1 + \varepsilon^2 A_\varepsilon(z)\Big) \exp\big(i\varepsilon\varphi_\varepsilon(z)\big), \tag{8}$$

where now, both φ_ε and A_ε tend to 0 at spatial infinity. Then, formal computations (see [25], [26]), assuming that $A_\varepsilon \to A$ and $\varphi_\varepsilon \to \varphi$ in some suitable sense as $\varepsilon \to 0$, that is $c \to \mathfrak{c}_s$, show that A must be a solution to the solitary wave equation for the KP-I equation:

$$\partial_{z_1} A - \partial_{z_1}^3 A + 12 A \partial_{z_1} A + 2\partial_{z_2}^2 \partial_{z_1}^{-1} A = 0 \tag{9}$$

and

$$\mathfrak{c}_s A = \partial_{z_1} \varphi. \tag{10}$$

As $c \approx \mathfrak{c}_s$ travelling waves are expected to behave (in the good scaling) as the Lump, expected to be the ground state. For mathematical results on the solitary waves of KP-I, see [16]. Complete justifications of the KP-I solitary wave limit for the travelling waves of GP have been given in [5] and in [13] (for a general nonlinearity and dimensions two and three). We refer to figure 5 for a plot of the travelling wave on the JR branch for $c = 1.35 \approx \sqrt{2}$.

1.4. **Outline of the paper**

As we have seen, the asymptotic behaviour $c \to 0$ and $c \to \mathfrak{c}_s$ are well understood for the travelling waves of GP. The natural questions that arise are: if we know other solitary waves solutions to KP-I does this give branches of travelling waves for GP at least for $c \to \mathfrak{c}_s$? and if we know some solution to (6), does this give branches of travelling waves for GP at least for $c \to 0$? We answer positively to these questions. Due to the integrability of KP-I in 2D, see for instance [39], explicit solitary waves have been given in [32], yielding for GP the purple and green branches in our Energy-Momentum diagram (figure 2). The black and the yellow branches

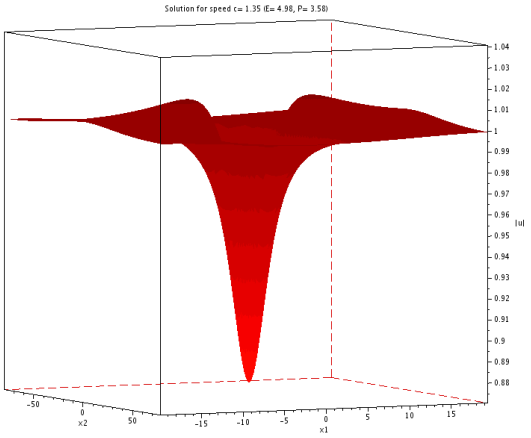

FIGURE 5. A rarefaction wave of the JR branch for $c = 1.35$

are associated with other solutions to (6), namely the configuration $(-2, +2)$ located at $Z_1 = -Z_2 = (0, 2)$ and the configuration $(-3, +3)$ located at $Z_1 = -Z_2 = (0, 3)$. To the best knowledge of the authors, these questions have no theoretical answer yet, and have not been investigated numerically.

In order to compute these new travelling waves, we will have to design a numerical framework to approximate solutions of $\mathrm{TW_c}$. Accordingly, section 2 will be dedicated to set up the needed numerical tools. The strategy follows closely [25] and [15]. Then, we will address in section 4 the question raised by the KP-I limit $c \to \mathfrak{c}_s$. We first describe the considered excited solitary waves given in [32]; we will furthermore take advantage of the fact that these waves belong to a larger family of solitary waves, as noticed in [22] (see also [20]), see section 3. Along the way, we wonder about their characteristics in the KP-I equation and propose to compute their numerical Morse index. We will thus consider the linearised KP-I equation for which we will compute the discrete eigenvalues within the numerical framework described in section 2. Finally, in section 5, we investigate the other vortex configurations $(+2, -2)$ and $(+3, -3)$.

2. NUMERICAL TOOLS

2.1. **Discretization framework**

First, we map $\mathbb{R}^2$ onto the square $[-\pi/2, \pi/2]^2$ using stretched coordinates as follows

$$R_1 x_1 = \tan(\hat{x}_1), \qquad R_2 x_2 = \tan(\hat{x}_2), \tag{11}$$

where $(x_1, x_2) \in \mathbb{R}^2$, $(\hat{x}_1, \hat{x}_2) \in [-\pi/2, \pi/2]^2$, and R_1 and $R_2 > 0$ are adapted to the lengthscales of the solution we are interested in. This mapping avoids working on an unbounded computational domain, hence the introduction of artificial boundary conditions. This type of coordinates change has since a long time been assessed in the area of general relativity through the approach of Penrose to conformally map infinite space-time to a finite region through a mapping of the space-time metric [33]. The precise type of compactification that we consider in this work has been successfully applied in the latter context in *e.g* [18] or in our precise context in [25]. The authors also used them in [15] in order to compute branches of travelling waves solution of the nonlinear Schrödinger equation for various type of nonlinearities. Finally, at the boundary of $[-\pi/2, \pi/2]^2$, we impose a Dirichlet boundary condition.

Another advantage of these stretched variables is that they allow to adapt to the typical lengthscales of the asymptotic regimes $c \approx 0$ or $c \approx \mathfrak{c}_s$. Indeed the two parameters (R_1 and R_2) define the two lengthscales in the two space variables. This is by adjusting these two parameters that we can check that the error at infinity is always much smaller than at finite distance from the origin (see [15] for details). More precisely, as the speed increases to $\mathfrak{c}_s$, the region of interest (where the solution has significant variation) is expanding towards infinity. Thus in order to ensure that we capture these variations with a good precision in the stretched variable, we reduce the values of R_1 and R_2 as the speed increases.

Any continuous problem is therefore first recast into this set of stretched variables and then solved numerically. The computational domain (i.e. the square $[-\pi/2, \pi/2]^2$) is discretized by a cartesian grid, with $N_1 \in \mathbb{N}^*$ points in the direction $\hat{x}_1$ and $N_2 \in \mathbb{N}^*$ points in the direction $\hat{x}_2$. A uniform discretization (*i.e.* $N := N_1 = N_2$) will be preferably chosen. We denote by h the size of the mesh (*i.e.* here $h = \pi/N$).

Each differential operator is expressed in the stretched coordinates (11) and then discretized within the Finite Difference framework. We refer to [15] for further details. Two types of discrete problems have to be considered. They are sketched in the two following subsections.

2.2. **Discrete eigenvalue problems**

First, we propose to compute the numerical Morse index of some explicit travelling wave solution of KP-I. Therefore we discretize the linearised KP-I differential operator around the corresponding solution. This leads to a discrete eigenvalue problem. More precisely, we have to solve a generalized eigenvalue problem of the following type

$$A_h u_h = \lambda_h B_h u_h, \tag{12}$$

with A_h and B_h two symmetric matrices. We refer the reader to subsection 3 for more details. We developed a Python code and computed the eigenvalues and eigenvectors using Scipy modulus [36].

2.3. **Numerical travelling wave solutions**

The second type of problem consists in computing, for a given speed $c > 0$, the numerical solution of $\mathrm{TW_c}$. We emphasize the dependence of the solution u in speed c in the equation $\mathrm{TW_c}$. This writes:

$$ic\partial_{x_1} u(c) - \Delta u(c) + u(c)(|u(c)|^2 - 1) = 0. \tag{13}$$

We shall impose the symmetries

$$u(x_1, x_2) = u(x_1, -x_2) = \bar{u}(-x_1, x_2). \tag{14}$$

Our goal is thus to compute the solution of (13), $u(c)$ at each speed c. To this end, we will either work with Newton's method or a continuation method as in [17] and as recalled in the following subsection. The main principle is to start from a solution for speed c and use it to compute the solution at speed $c + \delta c$ for δc small.

2.3.1. *Newton's method*

We consider the continuous stretched formulation of (13) (i.e. in the system of coordinates (11)). Each stretched differential operator is discretized with finite differences. This induces the discrete nonlinear system for $u_{c,h}$ (the approximation of u_c):

$$\mathcal{T}_{c,h}(u_{c,h}) = 0. \tag{15}$$

Then the algorithm is simply:

- Initialization: $\varepsilon > 0$, $c_0 > 0$, $u_{c_0,h}$ given.
- Iteration: $u_{c,h}$ given, find $u_{c+\delta c,h}$ solution of $\mathcal{T}_{c+\delta c,h}(u_{c+\delta c,h}) = 0$ with Newton's algorithm.
  (a) Initialization: $u^0 = u_{c,h}$,
  (b) Iteration: Do $u^{k+1} = u^k - D\mathcal{T}_{c+\delta c,h}(u^k)^{-1}.\mathcal{T}_{c+\delta c,h}(u^k)$, $k \leftarrow k+1$, until $\dfrac{|\mathcal{T}_{c+\delta c,h}(u^k)|}{\|\partial^h_{x_1} u^k\|} \leqslant \varepsilon$,
  (c) $k_{stop} := k$,

(d) $u_{c+\delta c,h} = u^{k_{stop}}$
- $c \leftarrow c + \delta c$

Newton's method has the advantage to be very efficient (when it converges) with a control over the residual of the equation (typically, in the computations, we achieve $\varepsilon = 10^{-8}$). However, Newton's method can require several iterations to converge (which in turn implies to solve the linear system several times in step (b)) and can also fail to compute a solution especially in the transonic limit. So that the recourse to another method is mandatory.

2.3.2. *Continuation method*

Inspired by [17], we formally differentiate (13) with respect to the speed c to obtain:

$$\Upsilon_c \left(\frac{\partial u}{\partial c}(c) \right) = i\partial_{x_1} u(c) \tag{16}$$

where

$$\Upsilon_c(v) \stackrel{\text{def}}{=} \Delta v - 2u(c)\langle u(c), v\rangle + (1 - |u(c)|^2)v - ic\partial_{x_1} v \tag{17}$$

is the linearised operator around $u(c)$. Equation (16) is viewed as an Ordinary Differential Equation determining $\dfrac{\partial u}{\partial c}$, provided we may invert Υ_c. We refer the reader to [15] for a discussion on this topic.

We compute the associated discrete operator $\Upsilon_{c,h}$ (associated to Υ_c) in the stretched variables using the Finite Difference framework proposed in subsection 2.1) and follow an iterative procedure.

- Initialization: $c_0 > 0$, $u_{c_0,h}$ given.
- Iteration: $u_{c,h}$ given, find $u_{c+\delta c,h}$ solution of (13).
  (a) Compute $\partial_c^h u := \Upsilon_{c,h}^{-1} \left(i\partial_{x_1}^h u_{c,h} \right)$ with $\partial_{x_1}^h$ the finite difference discretization of ∂_{x_1} in the stretched variables. This requires to solve one linear system.
  (b) Update the solution to $u_{c+\delta c,h}$ for the speed $c + \delta c$, with $u_{c+\delta c,h} = u_{c,h} + \delta c\, \partial_c^h u$.
- $c \leftarrow c + \delta c$

At each step, one has to solve a linear system, and in the transonic limit, the latter can be hard to solve (see the discussion in section 3.5. of [15]). Contrary to Newton's method, step (a) requires only one system resolution, but we do not have any control on the residual. However even if we do not impose a control on this residual directly with the continuation method, it allows, with a good initial residual (*i.e.* at the beginning of the iteration procedure), to compute an accurate solution everywhere and especially in regions where Newton's method may fail to converge. Since this numerical strategy has already been studied and validated in [15], we choose not to give extensive details and refer the reader to the latter reference.

2.3.3. *Strategy*

To summarize, we adopted the following strategy to compute the solution u on a whole interval (c_0, c_f) (c_0, c_f) of speeds c:

- Initialization: For the given initial speed c_0, we provide an initial guess computed with either the ansatz (4) in section 1.2 or (8) in 1.3.
- Iteration: From the solution obtained at speed c, we obtain a solution at speed $c + \delta c$, with δc small, using either Newton's method or the continuation method.

In what follows, we didn't obtain better results with the continuation method compared to Newton's method. When Newton's method fails to converge, the continuation methods allowed us to continue (for a very little while) the iterations in speed c but at the price of a residual deterioration. All the computations have been done using a code that we developed in the framework of Scilab software [38].

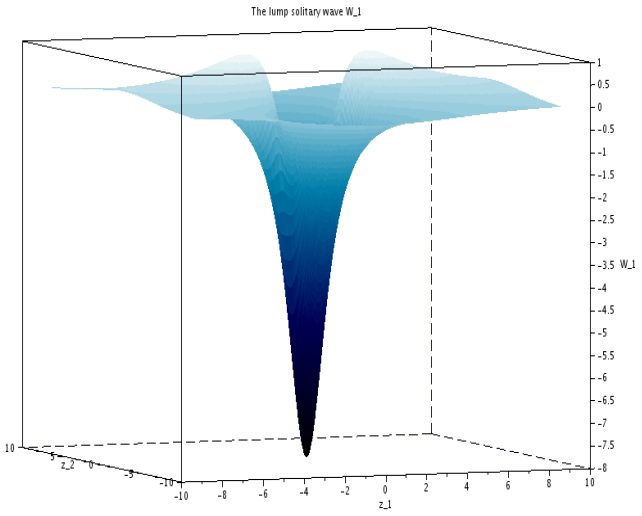

FIGURE 6. Representation of the first Lump solitary wave $\mathcal{W}_1$ of KP-I.

3. Explicit solitary waves solutions to KP-I and their numerical Morse index

3.1. **Explicit solitary wave solutions to KP-I**

We focus on the adimensionalized version of the solitary wave equation for KP-I given in (9):

$$\partial_{z_1}\mathcal{W} - \partial_{z_1}^3\mathcal{W} + \mathcal{W}\partial_{z_1}\mathcal{W} + \partial_{z_2}^2\partial_{z_1}^{-1}\mathcal{W} = 0. \tag{SW}$$

from which A (as defined in section 1.3) is recovered through the scaling

$$A(z_1, z_2) = \frac{1}{12}\mathcal{W}\Big(z_1, \frac{z_2}{\sqrt{2}}\Big). \tag{18}$$

We know that equation SW is integrable in 2D and that there exist explicit solutions. The first and well known one is the Lump solitary wave found in [29]. Its explicit expression is given as a z_1-derivative of a rational function as follows:

$$\mathcal{W}_1(z) = -12\partial_{z_1}^2 \ln\left(3 + z_1^2 + z_2^2\right) = -24\frac{3 - z_1^2 + z_2^2}{(3 + z_1^2 + z_2^2)^2}. \tag{19}$$

This solution is expected to be the ground state of SW, though, to the best knowledge of the authors, no proof is available. See figure 6 for a graphical representation. The rarefaction wave of the JR branch of travelling waves for GP plotted in figure 5 is clearly related to the $\mathcal{W}_1$ lump through the ansatz (8) and the scaling (7).

Furthermore, other explicit solutions to this equation have been obtained by the Hirota method in [32]. The expression of the second Lump solution is given by

$$\mathcal{W}_2(z) = -12\partial_{z_1}^2 \ln\left((z_1^2 + z_2^2)^3 + 25z_1^4 + 90z_1^2z_2^2 + 17z_2^4 + 475z_2^2 + 1875\right). \tag{20}$$

See figure 7 for a graphical representation. This solitary wave was first observed numerically in [2]. The third

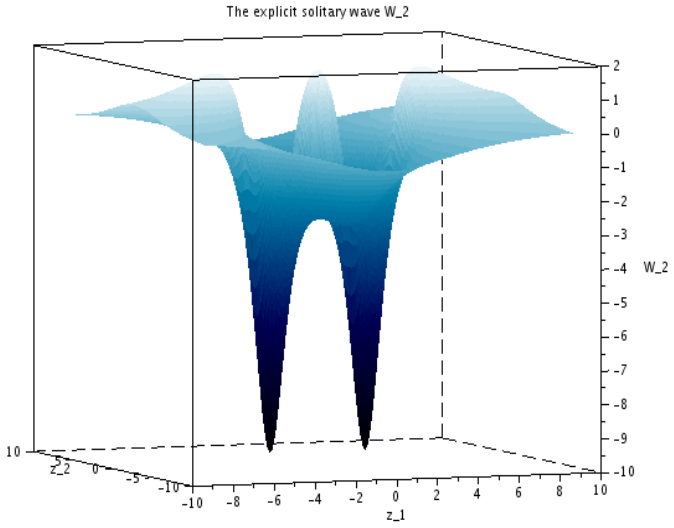

FIGURE 7. Representation of the second Lump solitary wave $\mathcal{W}_2$ of KP-I.

lump is given by

$$\mathcal{W}_3(z) = -12\partial_{z_1}^2 \ln\left((z_1^2+z_2^2)^6 + \ldots + \frac{159786550}{3}z_1^2 + \ldots + \frac{878826025}{9}\right). \tag{21}$$

See figure 8 for a graphical representation.

The reader may notice the increasing degree of the polynomial appearing in the expressions, that makes the computations harder and harder but theoretically feasible. One is expecting explicit solutions of higher "degrees" by continuing the arguments and computations of [32].

On the mathematical level, the only result the authors know about multiplicity results for solitary waves to the generalized KP-I equation (with nonlinearity $\mathcal{W}\partial_{z_1} f(\mathcal{W})$) is the paper [40], where the existence of at least two solitary waves is shown with the help of Lusternik-Schnirelman category.

Before concentrating on the possible branches of travelling waves solutions associated with these explicit KP-I solitary waves, we propose to study some of the properties of the latter through the computation of their numerical Morse index.

3.2. **Numerical Morse Index**

In order to compute the Morse index associated to each explicit solitary wave, we study the linearised operator around each explicit solution. The formal linearisation of the SW equation around one explicit solution $\mathcal{W}$ gives the operator $\mathscr{L}$:

$$\mathscr{L}(w) \stackrel{\text{def}}{=} w - \partial_{z_1}^2 w + \mathcal{W}w + \partial_{z_2}^2\partial_{z_1}^{-2}w. \tag{22}$$

The eigenvalue problem then reads

$$\mathscr{L}(w) = \lambda w. \tag{23}$$

In order to get rid of the non local term $\partial_{z_1}^{-2}w$, let us suppose that w writes as

$$w = \partial_{z_1}\Theta.$$

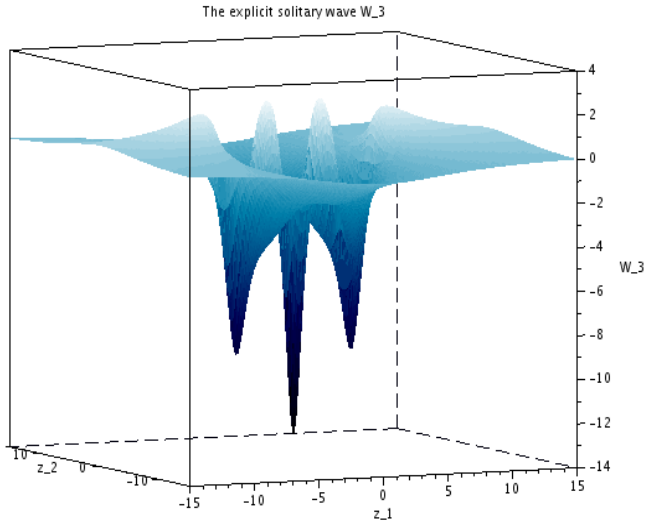

FIGURE 8. Representation of the third Lump solitary wave $\mathcal{W}_3$ of KP-I.

To stick with a variational formulation we then apply the operator ∂_{z_1} to the equation (23). This gives, denoting

$$\mathscr{L}_1(\Theta) \stackrel{\text{def}}{=} -\partial_{z_1}^2\Theta + \partial_{z_1}^4\Theta - \partial_{z_1}(\mathcal{W}\partial_{z_1}\Theta) - \partial_{z_2}^2\Theta, \tag{24}$$

the following eigenvalue problem

$$\mathscr{L}_1(\Theta) = -\lambda\partial_{z_1}^2\Theta. \tag{25}$$

The latter has a variational formulation, that is $\mathscr{L}_1$ and $\partial_{z_1}^2$ are symmetric.

Furthermore, clearly, $w_1 \stackrel{\text{def}}{=} \partial_{z_1}\mathcal{W}$ and $w_2 \stackrel{\text{def}}{=} \partial_{z_2}\mathcal{W}$ belong to $\ker(\mathscr{L})$, which means that for the lump $\mathcal{W}_1$ for instance,

$$\Theta_{1,1} = \mathcal{W}_1 = -24\frac{3 - z_1^2 + z_2^2}{(3 + z_1^2 + z_2^2)^2}$$

and

$$\Theta_{1,2} \stackrel{\text{def}}{=} 48\frac{z_1 z_2}{(3 + z_1^2 + z_2^2)^2}$$

belong to $\ker(\mathscr{L}_1)$. However, notice that in section 2.3, we impose the symmetries (14), so that the linear operators used in the algorithms are invertible. It was recently shown in [28] that the Kernel of the linearization near $\mathcal{W}_1$ is exactly two-dimensional, that is the only smooth solutions to $\mathscr{L}_{\mathcal{W}_1}(w) = 0$ such that $w \to 0$ at infinity are those in $\text{Span}(\partial_{z_1}\mathcal{W}_1, \partial_{z_2}\mathcal{W}_1)$. In the sequel, we concentrate on the eigenvalue problem (25) on the whole $\mathbb{R}^2$ without symmetry to characterize each explicit Lump solutions.

We follow the strategy of discretization explicited in section 2. In other words, we recast the continuous equations in the set of stretched variables. Doing so, the variational structure of the equations is kept in a discrete weighted L^2 space.

In the discrete setting, we then use classical centered finite difference formula and discrete integration by parts.

We are thus led to the discrete generalized eigenvalue problem that corresponds to the discrete version of (25): *Find* (λ_h, v_h) *such that*

$$A_h v_h = \lambda_h B_h v_h, \tag{26}$$

with A_h and B_h two symmetric matrices. In particular, the eigenvectors we represent are the Θ's.

We present in table 1 some of the eigenvalues we obtain (from the smaller ones) for the first three Lump solitary waves presented in this work. For each case, we clearly distinguish between negative eigenvalues (in

$\mathcal{W}_1$	$\mathcal{W}_2$	$\mathcal{W}_3$
-2.3539	-3.5842	-4.5767
	-2.5724	-3.4423
-1.67e-04	-0.8433	-2.6165
-1.08e-04	-0.3267	-1.3121
		-1.1904
0.677780	-8.775e-03	- 0.7577
0.865454	-5.521e-03	- 0.4686
	-2.592e-03	-0.3815
	-5.57e-04	-0.2185
	0.2681	-6.908e-03
	0.4564	-4.342e-03
	0.5872	-2.793e-03
	0.7915	-1.535e-03
	0.8005	-1.518e-03
	0.8229	-0.223e-03
	0.9819	
	0.9846	0.1796
	0.9912	0.2868
	0.9965	0.3405

TABLE 1. First numerical eigenvalues for the first three lump solitary waves. The discretization parameters have been set to $R_1 = R_2 = 0.2$ and $N = 1000$.

red), zero eigenvalues (with multiplicity, in blue) and positive ones (in black). We also provide some eigenvectors (see figure 9 for $\mathcal{W}_1$, figures 10 for $\mathcal{W}_2$ and figures 11 for $\mathcal{W}_3$). The computation was done using $N = 1000$ points and the numerical eigenvectors have been normalized in the ℓ^∞-norm.

Concerning the Kernel, we plotted in figure 9 the eigenvectors for $\mathcal{W}_1$ corresponding to the eigenvalues $-1.67e-04$ and $-1.08e-04$. We verified that they are identified (as expected) to $\Theta_{1,1}$ and $\Theta_{1,2}$. This is what was expected from [28]. Furthermore, we point out that the generalized eigenvalue problem $\mathscr{L}_1(\Theta) = -\lambda\partial_{z_1}^2\Theta$ is equivalent to the original one $\mathscr{L}(w) = \lambda w$, provided we work in the suitable energy space as described in [16]. In particular, the continuous spectrum is $[1, +\infty[$. On the discrete level, we can indeed check that -0.3267 and 0.2681 (for $\mathcal{W}_2$) and -0.2185 and 0.1796 (for $\mathcal{W}_3$) are indeed eigenvalues since, when the meshsize tends to 0, we can observe convergence to well-localized in space eigenvectors (see figures 10 and 11). In contrast and as expected, when $\lambda > 1$, we observed that eigenvectors are oscillating and not well-localized: see figure 12.

From the results in table 1, it follows that the Morse index and the dimension of the Kernel of the linearised operator $\mathscr{L}$ are as given in table 2. We find a Morse index equal to 1 for the first Lump $\mathcal{W}_1$, as expected if it is indeed a/the ground state for KP-I and then minimizes the energy at fixed momentum. From the above results, it is natural to *conjecture* that *the Morse index of the n-th Lump solitary wave* $\mathcal{W}_n$ *is* n^2 and that: *the linearised operator* $\mathscr{L}$ *around the n-th Lump solitary wave* $\mathcal{W}_n$ *has a Kernel of dimension* $2n$. This conjecture will be supported by arguments that will be given in the next section.

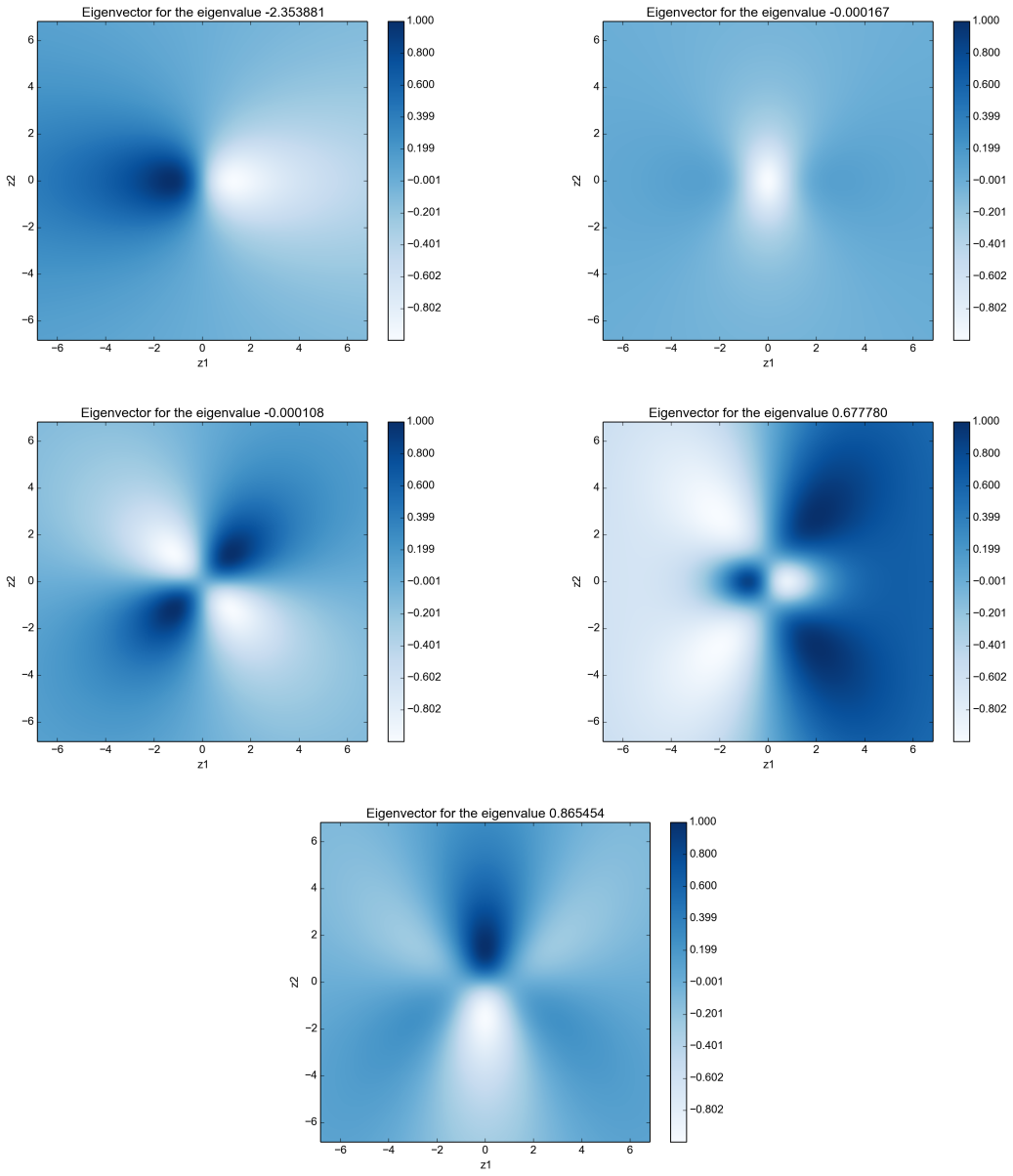

FIGURE 9. Normalized eigenvectors for $\mathcal{W}_1$, contourplot.

Lump solitary wave	Numerical Morse index	Dimension of the Kernel
$\mathcal{W}_1$	1	2
$\mathcal{W}_2$	4	4
$\mathcal{W}_3$	9	6

TABLE 2. Computation of the numerical Morse index and of the dimension of the Kernel.

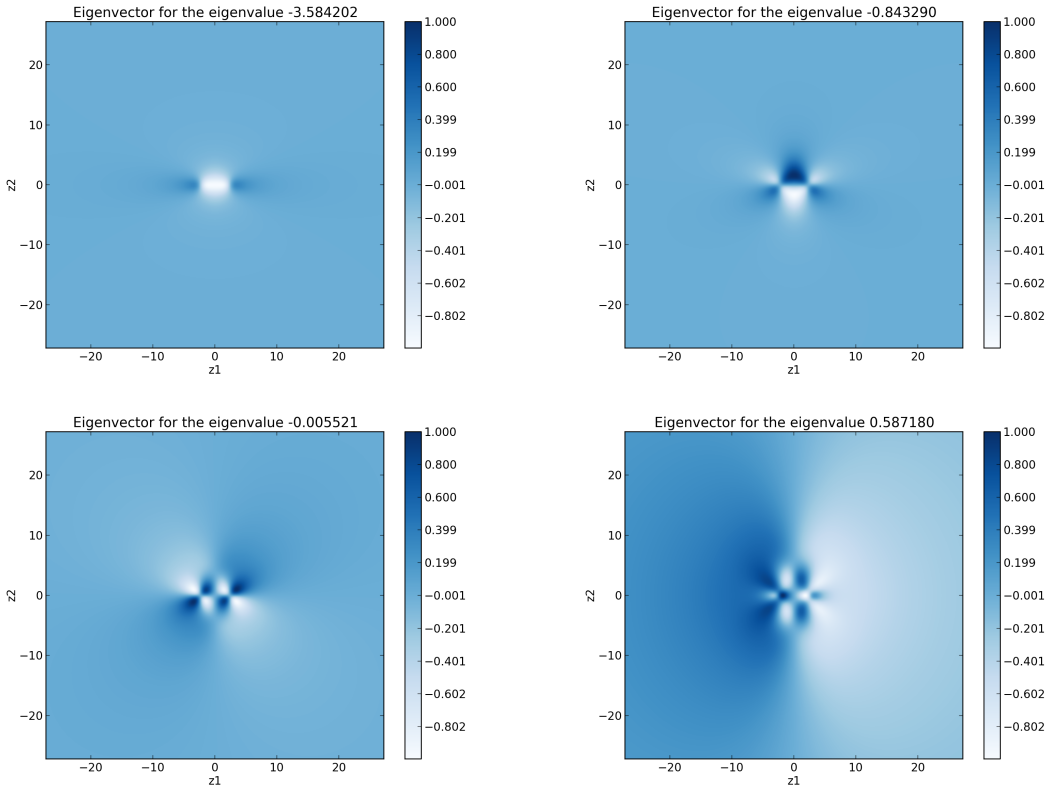

FIGURE 10. Some normalized eigenvectors for $\mathcal{W}_2$, contourplot.

3.3. **Parameter dependent families of multi Lump solutions**

In [22], the authors study steady states to KP-I and show that the Lump solitary wave $\mathcal{W}_2$ actually belongs to a two parameters family of solitary waves (the translations being removed) thus showing the degeneracy of $\mathcal{W}_2$. We corrected a small misprint in the formula given in [22] and provide a complete degeneracy result for $\mathcal{W}_2$ in the Proposition 1 below. The family is parametrized by the vectorial parameter $\boldsymbol{\alpha} = (\alpha_1, \alpha_2) \in \mathbb{R}^2$.

Proposition 1. *For any $\boldsymbol{\alpha} = (\alpha_1, \alpha_2) \in \mathbb{R}^2$, we define $\phi_2^{\boldsymbol{\alpha}}$ for $z = (z_1, z_2) \in \mathbb{R}^2$, by*

$$\begin{aligned}\phi_2^{\boldsymbol{\alpha}}(z) \stackrel{\text{def}}{=} (z_1^2 + z_2^2)^3 + 25z_1^4 + 90z_1^2z_2^2 + 17z_2^4 + \alpha_1 z_1^3 - 3\alpha_2 z_1^2 z_2 - 3\alpha_1 z_1 z_2^2 + \alpha_2 z_2^3 \\ - 125z_1^2 + 475z_2^2 - \alpha_1 z_1 - 5\alpha_2 z_2 + \alpha_1^2/4 + \alpha_2^2/4 + 1875. \qquad (27)\end{aligned}$$

For all $\boldsymbol{\alpha} \in \mathbb{R}^2$, the function $\phi_2^{\boldsymbol{\alpha}}$ is positive on $\mathbb{R}^2$, and one can define $\mathcal{W}_2^{\boldsymbol{\alpha}} \stackrel{\text{def}}{=} -12\partial_{z_1}^2 \ln \phi_2^{\boldsymbol{\alpha}}$. Then, $\mathcal{W}_2^{\boldsymbol{\alpha}}$ is a solution to SW. Moreover, we have that

(a) *the only polynomial functions ϕ of degree 6, positive, such that $-12\partial_1^2 \ln \phi$ is a (nonsingular) solution to SW are exactly those of the form $\mu\phi_2^{\boldsymbol{\alpha}}(z_1 - z_1^0, z_2 - z_2^0)$ for some $(z_1^0, z_2^0) \in \mathbb{R}^2$, $\mu > 0$ and $\boldsymbol{\alpha} \in \mathbb{R}^2$;*

(b) *for any $\boldsymbol{\alpha} \in \mathbb{R}^2$, the family of rational functions $(\partial_{z_1}\mathcal{W}_2^{\boldsymbol{\alpha}}, \partial_{z_2}\mathcal{W}_2^{\boldsymbol{\alpha}}, \partial_{\alpha_1}\mathcal{W}_2^{\boldsymbol{\alpha}}, \partial_{\alpha_2}\mathcal{W}_2^{\boldsymbol{\alpha}})$ is linearly independent,*

(c) *$\mathcal{W}_2^{(0,0)} = \mathcal{W}_2$, and in particular the Kernel of the linearised operator near $\mathcal{W}_2$ is at least of dimension 4.*

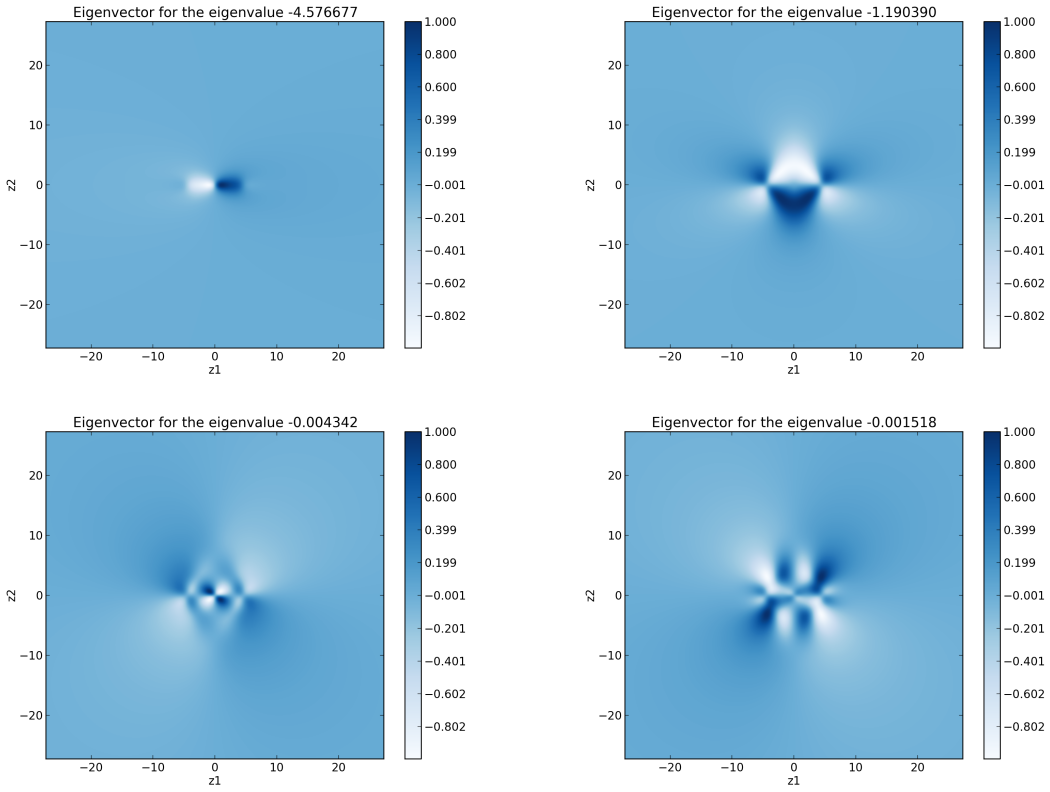

FIGURE 11. Some normalized eigenvectors for $\mathcal{W}_3$, contourplot.

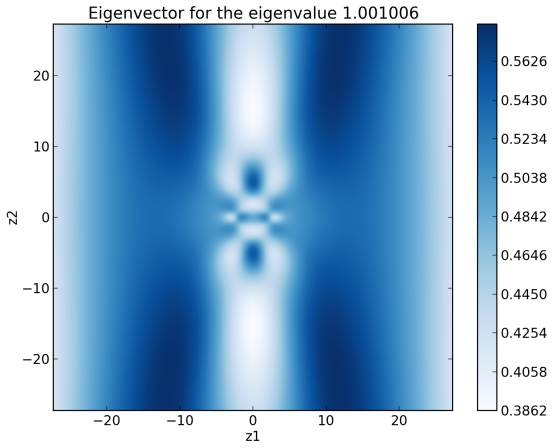

FIGURE 12. Normalized eigenvector for $\mathcal{W}_2$ corresponding to the eigenvalue $\lambda = 1.001$.

The misprint in [22] only concerns the terms $\alpha_1^2/4 + \alpha_2^2/4$. We also provide in appendix A the method that we used to obtain the formula and the positivity of $\phi_2^{\boldsymbol{\alpha}}$. For some of the pure algebraic computations, we used Maple Software.

Let us point out that the degeneracy result of item (c) follows from item (b) and is in accordance with the results obtained in the previous section.

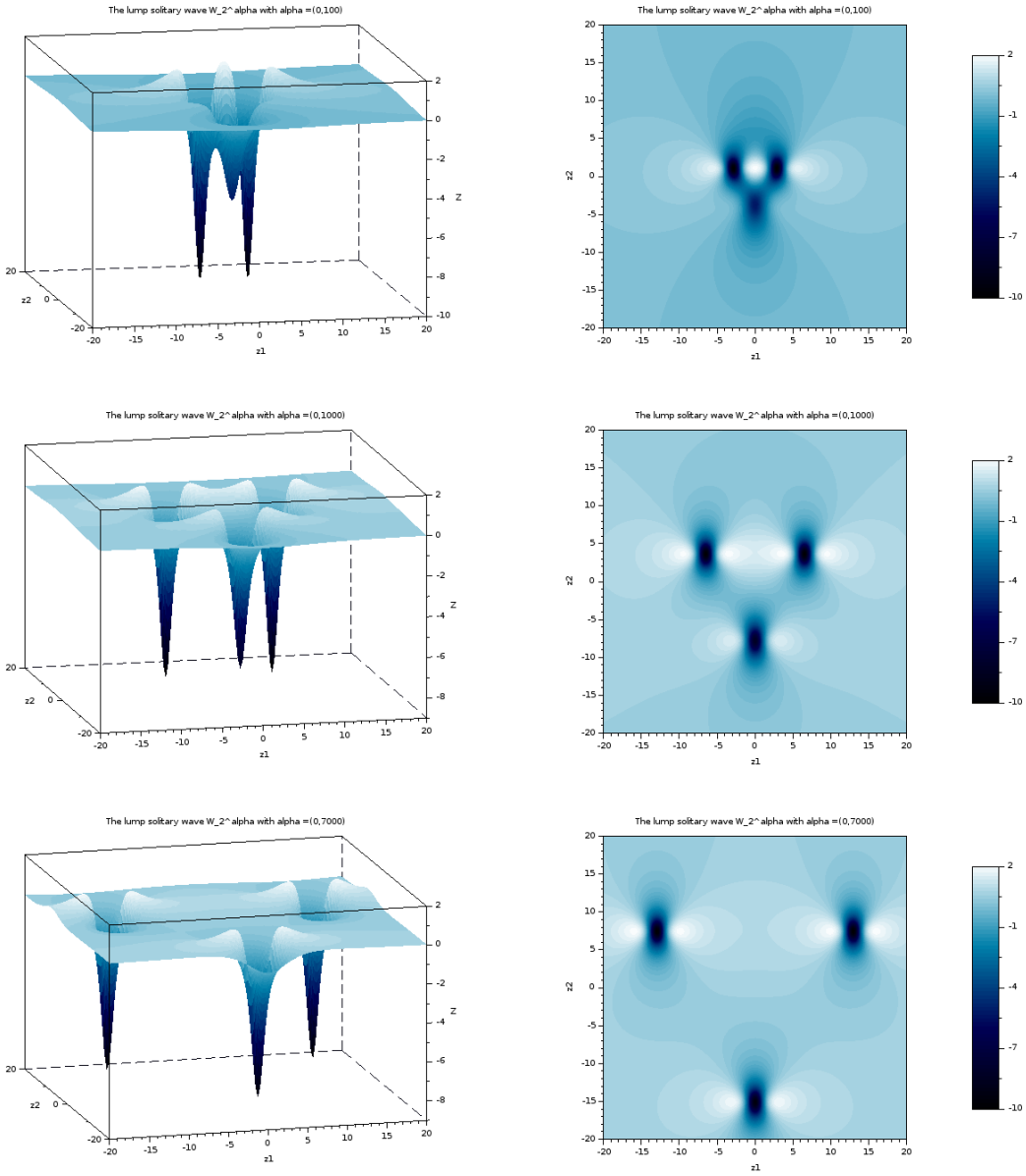

FIGURE 13. Solitary wave solution $\mathcal{W}_2^{\boldsymbol{\alpha}}$ for : (A) $\boldsymbol{\alpha} = (0, 100)$; (B) $\boldsymbol{\alpha} = (0, 1000)$; (C) $\boldsymbol{\alpha} = (0, 7000)$ On the left-hand side, surfacic plot; on the right-hand side, contourplot.

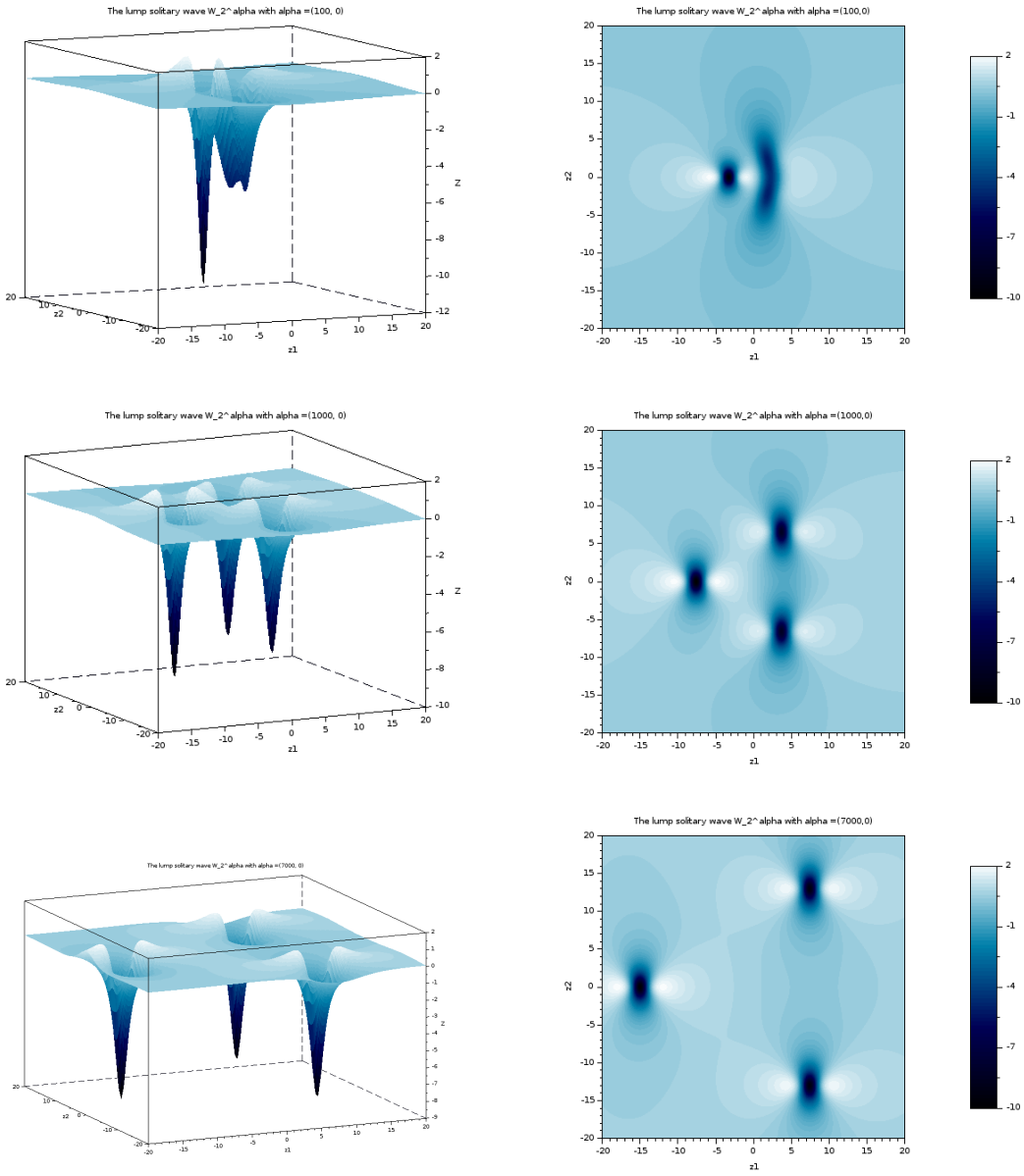

FIGURE 14. Solitary wave solution $\mathcal{W}_2^{\boldsymbol{\alpha}}$ for : (A) $\boldsymbol{\alpha} = (100, 0)$; (B) $\boldsymbol{\alpha} = (1000, 0)$; (C) $\boldsymbol{\alpha} = (7000, 0)$. On the left-hand side, surfacic plot; on the right-hand side, contourplot.

In figures 13 and 14, we represent for different values of the parameter $\boldsymbol{\alpha}$ the graph of $\mathcal{W}_2^{\boldsymbol{\alpha}}$ and its corresponding contour plot. As was observed in [22], the solution $\mathcal{W}_2^{\boldsymbol{\alpha}}$ evolves, when the free parameter $\boldsymbol{\alpha}$ is large, to three well separated $\mathcal{W}_1$ Lumps. In other words, $\mathcal{W}_2$ may be seen as some kind of superposition of three $\mathcal{W}_1$ Lumps. This observation is in agreement with the computation of the Morse index for several values of the parameters.

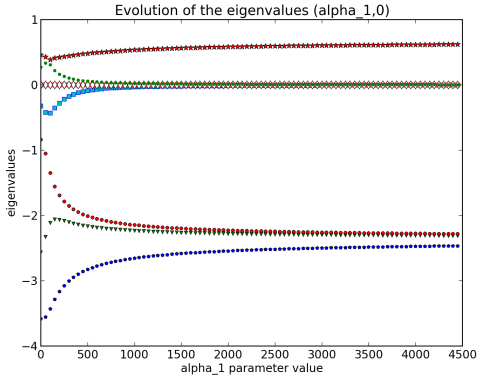

(A)

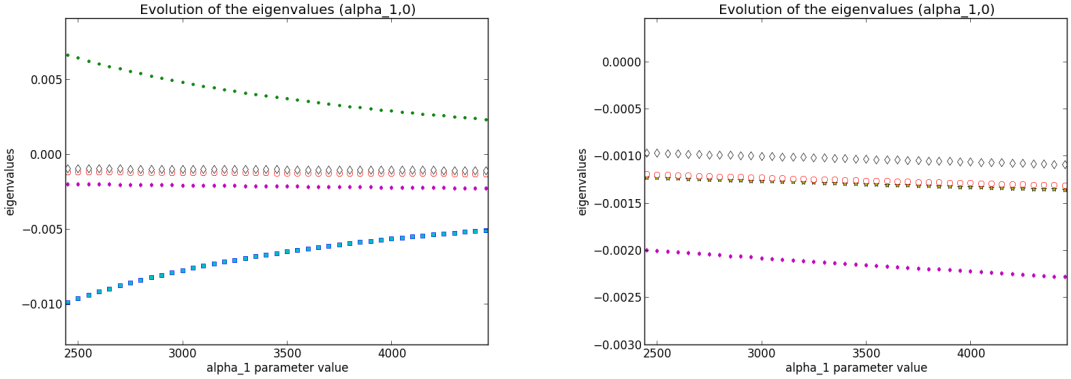

(B)

FIGURE 15. (A) Representation of the evolution of several eigenvalues of $\mathcal{W}_2^{\boldsymbol{\alpha}}$, with $\boldsymbol{\alpha} = (\alpha_1, 0)$, with respect to α_1; (B) Zoom for α_1 large and in the vicinity of zero. The numerical parameters have here been set to $R_1 = R_2 = 0.05$ and $N = 1500$.

We represent in figure 15, the evolution of the eigenvalues for several parameters $\boldsymbol{\alpha}$ of the form $(\alpha_1, 0)$, with $\alpha_1 > 0$. Here we choose to focus on one direction of variation for the parameter $\boldsymbol{\alpha}$ and positive values of the parameter α_1. Other cases gave the same qualitative behavior and, thus, interpretation. We start from the situation $\boldsymbol{\alpha} = (0, 0)$, with 4 negative numerical eigenvalues and a Kernel of dimension 4, and as α_1 becomes large the largest negative eigenvalue goes to zero, and the smallest positive one also. So that, for $\alpha_1 \to +\infty$, there is asymptotically 3 negative eigenvalues corresponding to the 3 well-separated $\mathcal{W}_1$ Lumps, with the negative eigenvalue ≈ -2.3539 of $\mathcal{W}_1$ and a Kernel of dimension 6 (that is 3 times the dimension of the Kernel of one individual $\mathcal{W}_1$ Lump). To support this analysis, we show on figure 16 the set of first normalized eigenvectors for parameter $\boldsymbol{\alpha} = (7000, 0)$.

The first normalized vector in figure 16 corresponding to the numerical eigenvalue -2.656372 is localized in the region of the (z_1, z_2)-plane of one of the asymptotic $\mathcal{W}_1$ Lump, and furthermore resemble the eigenvector for the negative eigenvalue associated with $\mathcal{W}_1$ (see figure 9). The reader could furthermore convince himself that the difference between the second eigenvector (for the numerical eigenvalue ≈ -2.234496) and the third eigenvector (for the numerical eigenvalue ≈ -2.146401) gives a vector that is localized around another asymptotic $\mathcal{W}_1$ Lump solution that resemble the eigenvector for $\mathcal{W}_1$ negative eigenvalue. Analogous conclusion would hold for the sum. In figure 15, one notices that the smallest (negative) eigenvalue converges rather slowly to the negative

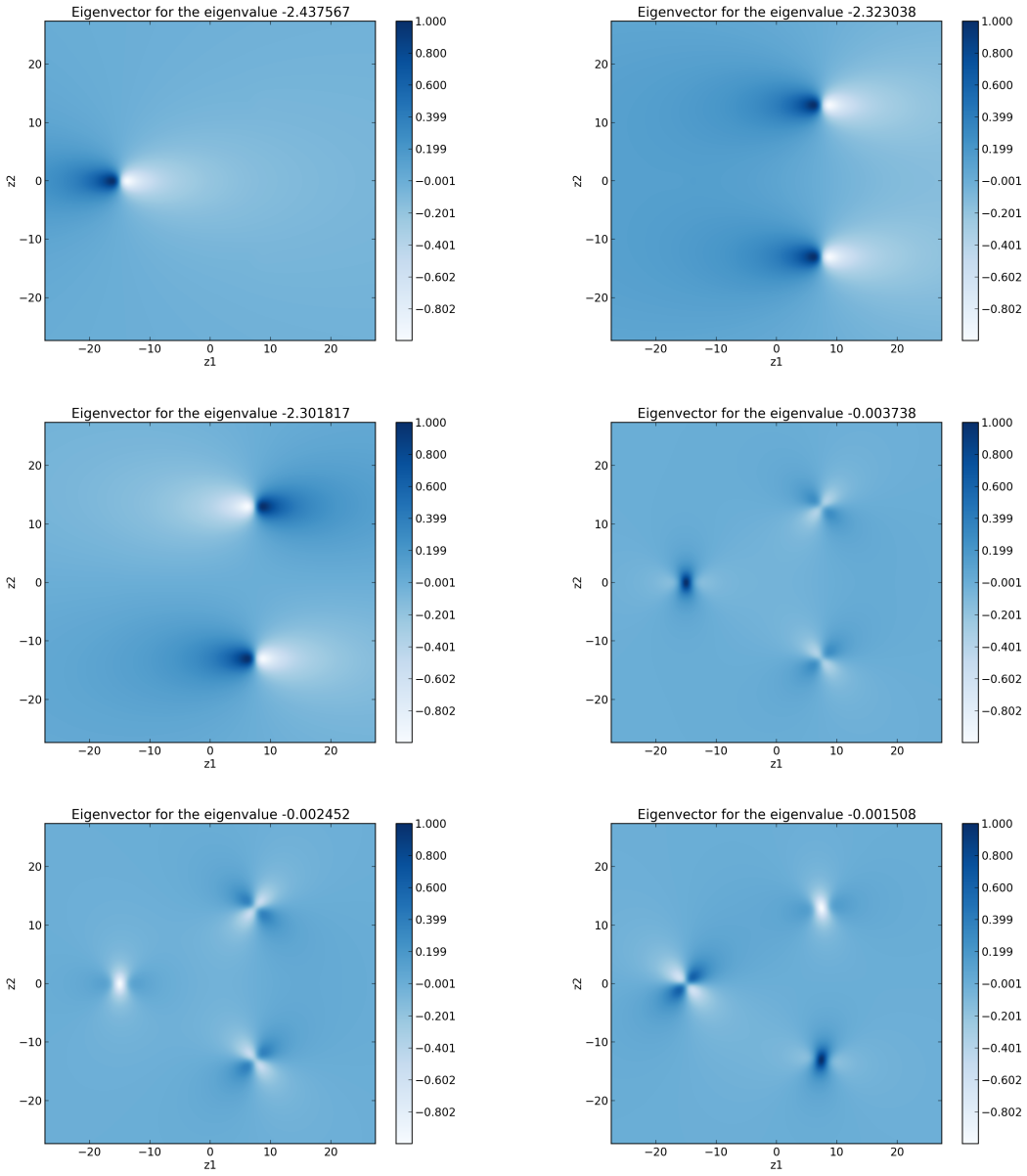

FIGURE 16. Normalized eigenvectors for $\boldsymbol{\alpha} = (7000, 0)$. The numerical parameters have here been set to $R_1 = R_2 = 0.05$ and $N = 1500$.

eigenvalue ≈ -2.3539 of $\mathcal{W}_1$, which is not surprising since the distance between the three $\mathcal{W}_1$ Lumps is of the order of $|\boldsymbol{\alpha}|^{1/3}$. Finally, at least at the numerical level, it seems that the family is iso-spectral.

These multiplicity results have been extended in [20], where, for each $N \in \mathbb{N}^*$, a set of rational singular solutions to KP-II is given; the denominator has degree $N(N+1)$ and involves $2N$ free parameters. The computations also work for KP-I, leading to the existence of such parameter solutions for the latter equation. In Proposition 2 below, we provide an explicit expression of a three parameters family of solutions to which $\mathcal{W}_3$

belongs to. This second family of solutions is indeed a 4-parameters dependent family that we express in terms of the vector $\boldsymbol{\beta} \in \mathbb{R}^4$. The expression has been obtained following the same lines as for $\mathcal{W}_2$ (see appendix A).

Proposition 2. *For any $\boldsymbol{\beta} = (\beta_1, \beta_2, \beta_3, \beta_4) \in \mathbb{R}^4$, we define $\phi_3^{\boldsymbol{\beta}}$ for $(z_1, z_2) \in \mathbb{R}^2$, by*

$$
\begin{aligned}
\phi_3^{\boldsymbol{\beta}}(z) \stackrel{\text{def}}{=}\ & (z_1^2+z_2^2)^6 + 2(z_1^2+z_2^2)^3(49z_1^4+198z_1^2z_2^2+29z_2^4) \\
& + \beta_1(z_1^9 - 6z_1^5z_2^4 - 8z_1^3z_2^6 - 3z_1z_2^8) - \beta_2(3z_1^8z_2 + 8z_1^6z_2^3 + 6z_1^4z_2^5 - z_2^9) \\
& + 735z_1^8 + 18620z_1^6z_2^2 + 37450z_1^4z_2^4 + 35420z_1^2z_2^6 + 4335z_2^8 \\
& + \beta_1(300z_1^5z_2^2 + 200z_1^3z_2^4 - 484z_1z_2^6) + \beta_2(60z_1^2z_2^5 + 40z_1^4z_2^3 - 404z_1^6z_2) \\
& + \beta_3(z_1^7 - 9z_1^5z_2^2 - 5z_1^3z_2^4 + 5z_1z_2^6) + \beta_4(z_2^7 - 9z_1^2z_2^5 - 5z_1^4z_2^3 + 5z_1^6z_2) \\
& + (75460/3 + 3\beta_1^2/20 + 7\beta_2^2/20)z_1^6 + (220500 + 9\beta_1^2/4 - 3\beta_2^2/4)z_1^4z_2^2 \\
& + (-14700 - 3\beta_1^2/4 + 9\beta_2^2/4)z_1^2z_2^4 + (798980/3 + 7\beta_1^2/20 + 3\beta_2^2/20)z_2^6 \\
& + \beta_1\beta_2(6z_1^5z_2/5 + 6z_1z_2^5/5 - 4z_1^3z_2^3) + (13\beta_3 - 102\beta_1)z_1^5 + (105\beta_4 - 9170\beta_2)z_1^4z_2 \\
& + (2440\beta_1 - 230\beta_3)z_1^3z_2^2 + (13000\beta_2 - 190\beta_4)z_1^2z_2^3 + (45\beta_3 - 2690\beta_1)z_1z_2^4 + (42\beta_2 - 7\beta_4)z_2^5 \\
& + (-5187875/3 + \beta_3\beta_1/2 - \beta_4\beta_2/2 - 69\beta_1^2/4 + 107\beta_2^2/4)z_1^4 \\
& + (16391725/3 - \beta_3\beta_1/2 + \beta_4\beta_2/2 + 139\beta_1^2/4 - 21\beta_2^2/4)z_2^4 + (\beta_1\beta_4 - 88\beta_2\beta_1 + \beta_2\beta_3)z_1^3z_2 \qquad (28) \\
& + (565950 + 3\beta_1^2/2 - 21\beta_2^2/2)z_1^2z_2^2 + (\beta_1\beta_4 - 104\beta_2\beta_1 + \beta_2\beta_3)z_1z_2^3 \\
& - (\beta_1^3/20 + 245\beta_3 + \beta_2^2\beta_1/20 + 13720\beta_1/3)z_1^3 + (84280\beta_2/3 - \beta_2\beta_1^2/20 - \beta_2^3/20 - 245\beta_4)z_2^3 \\
& + (76860\beta_2 + 3\beta_2\beta_1^2/20 + 3\beta_2^3/20 - 665\beta_4)z_1^2z_2 + (3\beta_1^3/20 + 535\beta_3 + 3\beta_2^2\beta_1/20 + 14460\beta_1)z_1z_2^2 \\
& + (-20\beta_3\beta_1 + 159786550/3 + 3137\beta_2^2/4 + 2205\beta_1^2/4 + \beta_3^2/4 + \beta_4^2/4 - 25\beta_4\beta_2)z_1^2 \\
& + (\beta_3^2/4 - 35\beta_3\beta_1 + 300896750/3 - 171\beta_2^2/4 + 4121\beta_1^2/4 + \beta_4^2/4 - 10\beta_4\beta_2)z_2^2 \\
& + (3\beta_1\beta_4 - 278\beta_2\beta_1 + 3\beta_2\beta_3)z_1z_2 \\
& + (-\beta_3\beta_1^2/20 + 12005\beta_3/3 + \beta_2^2\beta_3/20 - 131\beta_2^2\beta_1/20 + 708295\beta_1/3 + \beta_2\beta_1\beta_4/10 + 49\beta_1^3/20)z_1 \\
& + (\beta_2\beta_1\beta_3/10 - 151\beta_2\beta_1^2/20 + 18865\beta_4/3 - 2584505\beta_2/3 - \beta_2^2\beta_4/20 + 29\beta_2^3/20 + \beta_1^2\beta_4/20)z_2 \\
& - 213\beta_4\beta_2/2 + 878826025/9 + 3\beta_3^2/4 + \beta_2^2\beta_1^2/200 - 57\beta_3\beta_1/2 \\
& + 3\beta_4^2/4 + 57227\beta_2^2/12 + \beta_1^4/400 + \beta_2^4/400 + 15043\beta_1^2/12.
\end{aligned}
$$

We define $\mathcal{P}_3 \stackrel{\text{def}}{=} \{\boldsymbol{\beta} \in \mathbb{R}^4 \text{ s.t. } \inf_{z\in\mathbb{R}^2} \phi_3^{\boldsymbol{\beta}}(z) > 0\}$. $\mathcal{P}_3$ is an open set containing $\boldsymbol{\beta} = (0,0,0,0)$. For all $\boldsymbol{\beta} \in \mathcal{P}_3$, one defines $\mathcal{W}_3^{\boldsymbol{\beta}} \stackrel{\text{def}}{=} -12\partial_{z_1}^2 \ln \phi_3^{\boldsymbol{\beta}}$. Then $\mathcal{W}_3^{\boldsymbol{\beta}}$ is a solution to SW. Moreover, we have that

(a) *the only polynomial functions ϕ of degree 12, positive, such that $-12\partial_1^2 \ln \phi$ is a (nonsingular) solution to SW are exactly those of the form $\mu\phi_3^{\boldsymbol{\beta}}(z_1 - z_1^0, z_2 - z_2^0)$ for some $(z_1^0, z_2^0) \in \mathbb{R}^2$, $\mu > 0$ and $\boldsymbol{\beta} \in \mathcal{P}_3$.*

(b) *for any $\boldsymbol{\beta} \in \mathbb{R}^4$, the family of rational functions $(\partial_1\mathcal{W}_3^{\boldsymbol{\beta}}, \partial_2\mathcal{W}_3^{\boldsymbol{\beta}}, \partial_{\beta_1}\mathcal{W}_3^{\boldsymbol{\beta}}, \dots, \partial_{\beta_4}\mathcal{W}_3^{\boldsymbol{\beta}})$ is linearly independent.*

(c) *$\mathcal{W}_3^{(0,0,0,0)} = \mathcal{W}_3$. In particular, the Kernel of the linearised operator near $\mathcal{W}_3$ is of dimension at least 6.*

Let us point out that item (c) is in accordance with the results obtained in the previous section. In Figure 17, we pick two relevant values of the parameter $\boldsymbol{\beta}$ and represent the corresponding solution $\mathcal{W}_3^{\boldsymbol{\beta}}$. Similar behaviour (as in the case of $\mathcal{W}_2^{\boldsymbol{\alpha}}$) appears: the solution $\mathcal{W}_3^{\boldsymbol{\beta}}$ evolves, when the free parameter $\boldsymbol{\beta}$ is large, to six well separated $\mathcal{W}_1$ lumps. This observation is in agreement with the results of the computation the Morse index for several values of the parameters, where we observe the same qualitative behaviour as for $\mathcal{W}_2^{\boldsymbol{\alpha}}$. In all cases, we start from the situation $\boldsymbol{\beta} = (0,0,0,0)$, with 9 negative eigenvalues and a kernel of dimension 6, and as $\boldsymbol{\beta}$ becomes large the three largest negative eigenvalue goes to zero, and the three smallest positive one also.

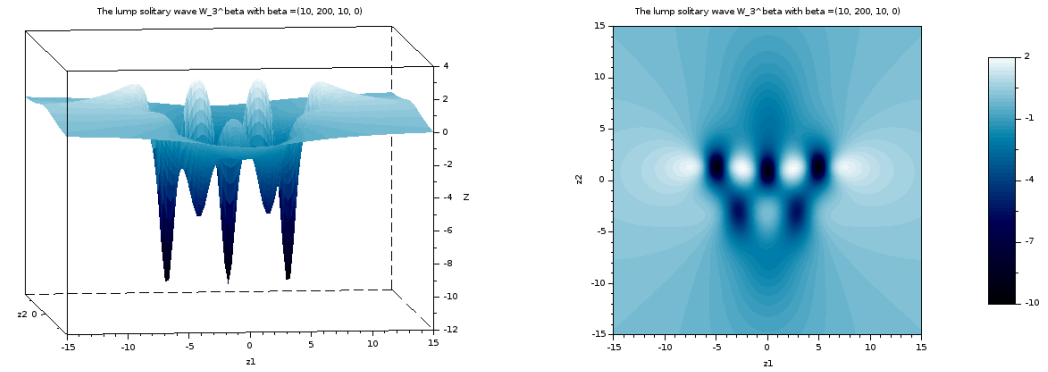

(A)

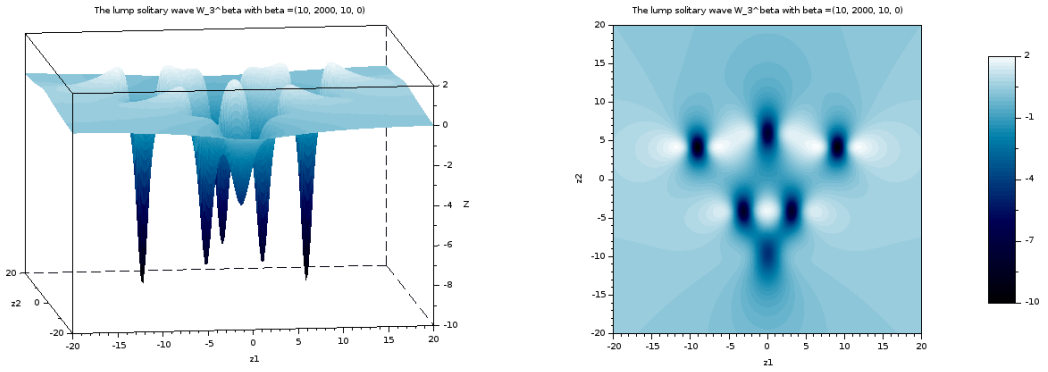

(B)

FIGURE 17. Solitary wave solution $\mathcal{W}_3^{\boldsymbol{\beta}}$ for : (A) $\boldsymbol{\beta} = (10, 100, 10, 0)$; (B) $\boldsymbol{\beta} = (10, 2000, 10, 0)$. On the left-hand side, surfacic plot; on the right-hand side, contourplot.

So that, for $|\boldsymbol{\beta}| \to +\infty$, there is asymptotically 6 negative eigenvalues (corresponding to the 6 $\mathcal{W}_1$ Lumps, with the eigenvalue ≈ -2.3539) and a Kernel of dimension 12 (that is 6 times the dimension of the Kernel of one individual $\mathcal{W}_1$ Lump). We also observed the same behaviour as $\boldsymbol{\beta}$ becomes large regarding to the localization of the eigenvectors around the regions where the 6 the asymptotic Lumps $\mathcal{W}_1$ seem to localize as in the case of $\mathcal{W}_2^{\boldsymbol{\alpha}}$. We thus do not reproduce the plots and analysis here.

We now continue with the study of multiple branches of travelling wave solution to GP issued from the explicit KP-I solitary waves. We shall actually focus only on the solutions $\mathcal{W}_2$ and $\mathcal{W}_3$ exhibited in section 3.1. The analogous question for the whole parameter dependent family of solutions $\mathcal{W}_2^{\boldsymbol{\alpha}}$ and $\mathcal{W}_3^{\boldsymbol{\beta}}$ presented in this section is out of the scope of this article, but will be investigated in the future. Indeed, whereas for $\mathcal{W}_2$ and $\mathcal{W}_3$ the Kernel can be removed thanks to the imposed symmetries, the question of the degeneracy for the parameter dependent solutions will deserve a specific study.

4. Other branches of travelling wave solutions to GP with KP-I asymptotics

4.1. The Energy-Momentum diagram for GP in 2D: the JR branch

We begin with the well known case of the JR branch of travelling waves obtained in [25], for which the Energy-Momentum diagram is given in Figure 1. This branch is characterized by two vortices for $c \approx 0$ and by the KP-I asymptotic limit associated with the $\mathcal{W}_1$ Lump solitary wave when $c \approx \mathfrak{c}_s$. Actually, one may obtain numerically this branch starting either from $c \approx \mathfrak{c}_s$ and an approximate solution given by (8)-(10) with A related to the Lump solitary wave $\mathcal{W}_1$ through (18), either from $c \approx 0$ and an approximate solution given by (4), provided we have an approximation of the vortex profile $\mathfrak{a}_1$ (see subsection 5.1). For details, we refer the reader to [25] and [15]. We give two types of representations of the travelling waves solutions on the JR branch. In figure 18, we plot, for various speeds c, on the right-hand side, the $3d$ plot of the modulus of the travelling wave in the domain $\{x_1 \geqslant 0\}$ (in the domain $\{x_1 \leqslant 0\}$, it suffices to use the symmetry (14)) and on the left-hand side the corresponding position on the Energy-Momentum diagram. Figure 19 contains contour plot views on the whole plane $\mathbb{R}^2$. One clearly sees the evolution as the speed of the wave increases: for $c \approx 0$, we have two well-separated vortices at distance $\approx 1/c$ one from another; they get closer when c increases and at some step merge, and for higher speeds, vorticity is lost; for $c \approx \mathfrak{c}_s$, the modulus is uniformly close to 1 and the travelling wave is a rarefaction pulse as in figure 5.

On the numerical level, two approaches can be used to obtain this branch. The first one, used in [25], is based on Newton's algorithm (see subsection 2.3); the other one is based on the variational properties of the problem and looks for finding (local) minimizers to suitable functionals (*cf.* [15]). The local minimizing technique has many advantages over a continuation method; it is quick, systematic (relying on a heat flow technique) and precise (see [15] for details). However, to try to catch numerically the other possible branches of solutions arising from the second and third Lump as described in section 3, we can not rely on such a minimization procedure. Therefore, we focus on continuation type methods as described in subsection 2.3.

4.2. New branch of travelling waves associated with the second lump $\mathcal{W}_2$

Let us concentrate on the second Lump $\mathcal{W}_2$, that has the expression (20). We use the scalings (7) and initialize a continuation method with $c \approx \mathfrak{c}_s$ *via* the ansatz (8)-(10) and employing (20).

We plot the resulting Energy-Momentum diagram in Figure 20. The blue curve is the JR branch with the transonic limit given by the $\mathcal{W}_1$ Lump (see subsection 4.1). The purple curve represents the Energy-Momentum diagram obtained starting from the KP-I limit with the second Lump $\mathcal{W}_2$.

Figures 21 and 22 depict the evolution of the modulus of the numerical travelling wave solution for various (decreasing) speeds. In figure 23, we give the corresponding contourplots. Similarly to the ground state branch, the minimum value of the modulus of the solution decreases until vortices appear by pairs. For $c = 0.73$, we see four vortices, and for c further decreasing, the local minimum of the modulus on the x_2 axis decreases down to zero and then two additional vortices appear: we end-up with six distinguishable vortices.

4.3. New branch of travelling waves associated with the third lump $\mathcal{W}_3$

We now turn to the third Lump solitary wave $\mathcal{W}_3$ given by (21). Analogously, we make use of (7) and initialize the continuation with $c \approx \mathfrak{c}_s$ *via* the ansatz (8). We plot the resulting Energy-Momentum diagram in Figure 24.

We obtain a third branch of travelling waves solutions. Figures 25 and 26 describe the evolution of the modulus of the computed travelling wave solution that we compute. In a similar fashion, the minimum and local minima of the modulus decrease as the speed decreases down to the speed ≈ 0.9 (see Figure 26 (A)). Then, vortices appear and we observe the same kind of splitting phenomenon as for the branch associated with the second Lump. At speed ≈ 0.685, ten vortices are clearly distinguishable.

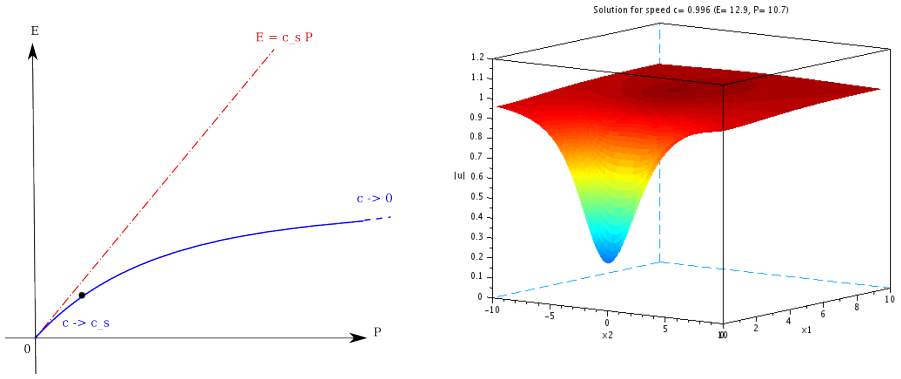

(A)

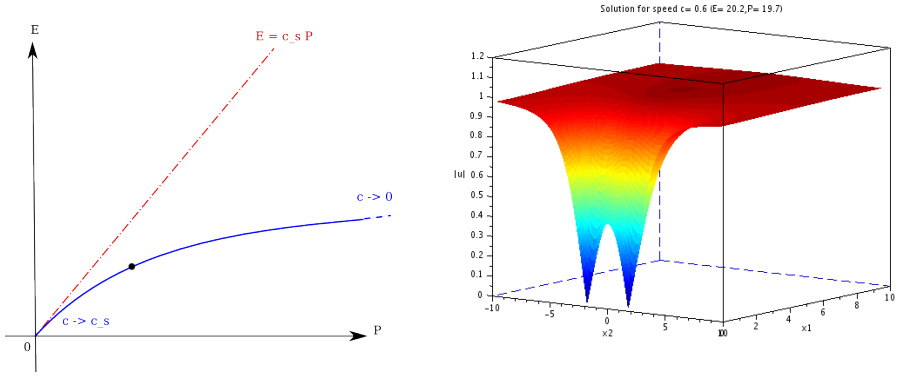

(B)

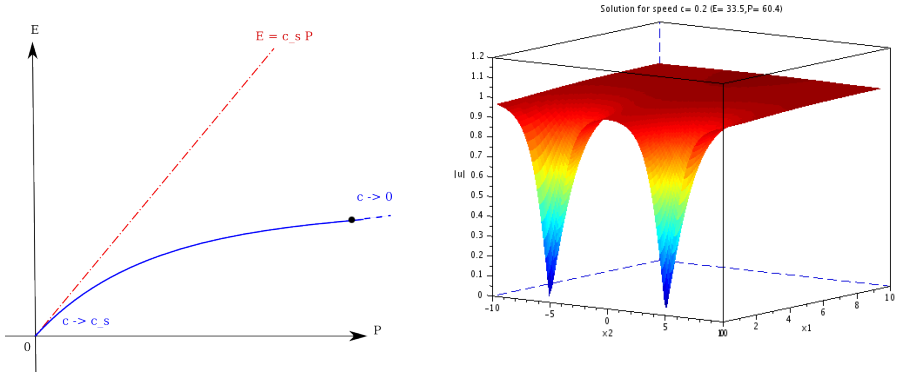

(C)

FIGURE 18. Travelling wave solution of the JR branch for speeds: (A) $c = 1$; (B) $c = 0.6$; (C) $c = 0.2$. On the left-hand side, position in the Energy-Momentum diagram (spotted with a black point); on the right-hand side, modulus.

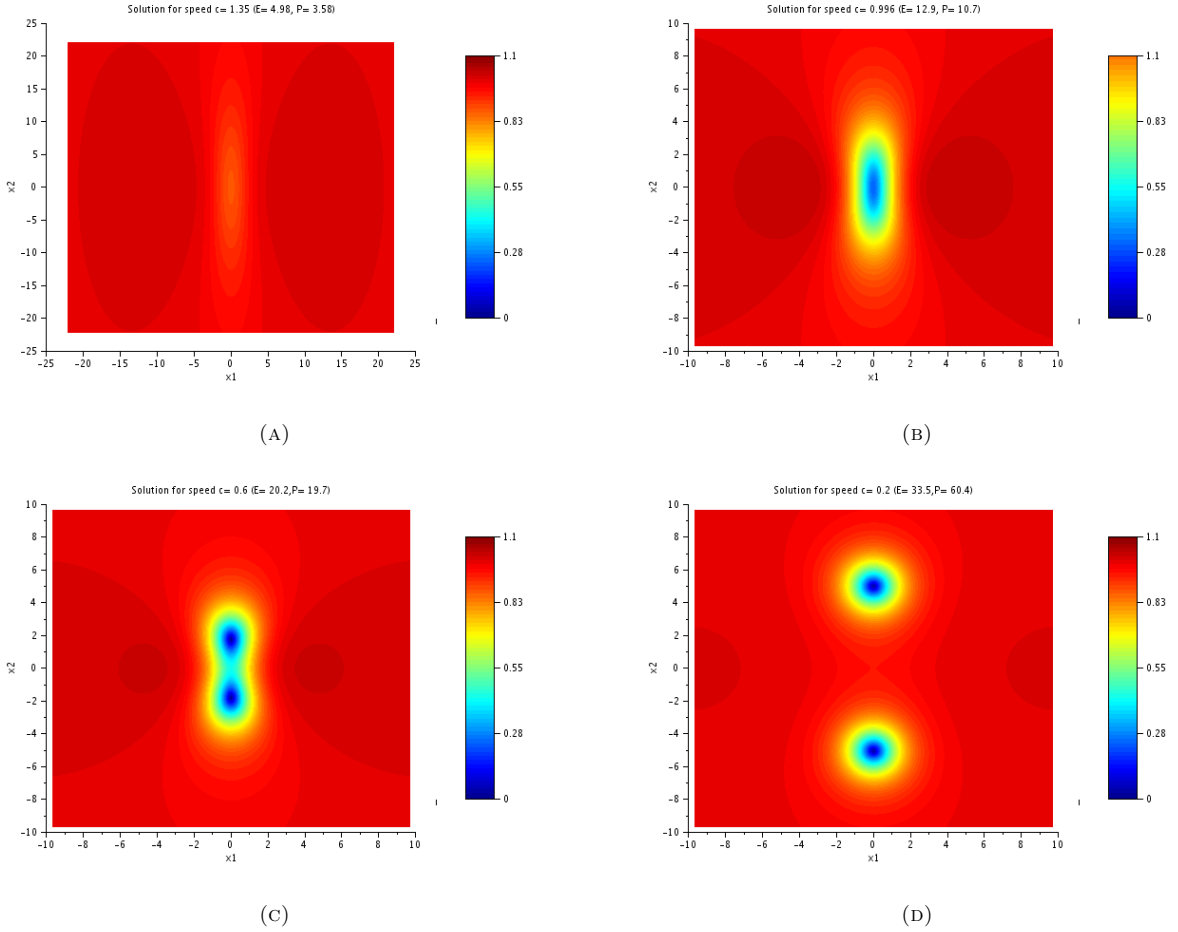

(A) (B)

(C) (D)

FIGURE 19. Contourplots of the travelling waves of the JR branch: (A) $c = 1.35$; (B) $c = 1$; (C) $c = 0.6$; (D) $c = 0.2$.

4.4. **Conclusion**

Our numerical simulation put forward two new branches of travelling wave solutions corresponding to excited states; these branches are distinct from the JR state branch and from each other. As can be checked in figures 19 (D), 23 (F) and 27 (F), we can *conjecture that the branch associated with the n-th Lump solitary wave* $\mathcal{W}_n$ *eventually exhibits* $2(2n-1)$ *vortices*. One can check that the degree of these vortices are ± 1 by considering the phase of the solution. The precise charge of each vortex is given in figure 28. In particular, we notice that for the JR branch as well as for the branches associated with the $\mathcal{W}_2$ and the $\mathcal{W}_3$ Lumps, the total charge in the upper half-space is always equal to one. This is in agreement with the fact that the number of vortices is of the form twice an odd integer.

For the $\mathcal{W}_2$ branch (resp. $\mathcal{W}_3$ branch), we have been able to reach the speed 0.27 (resp. 0.685). Below these speeds, our algorithms stop converging. In particular, we can not claim that the branch would continue up to small speeds solutions with well-separated vortices as for the JR branch. As a consequence, for the two endpoint travelling waves (for speeds 0.27 and 0.685), the term vortex only means a zero of the wave function, and we do not claim any approximation by the vortices $V_{\pm 1}$ (which is valid only for small c). Another argument suggesting that it is not reasonnable to expect travelling waves with small speeds for the branches associated

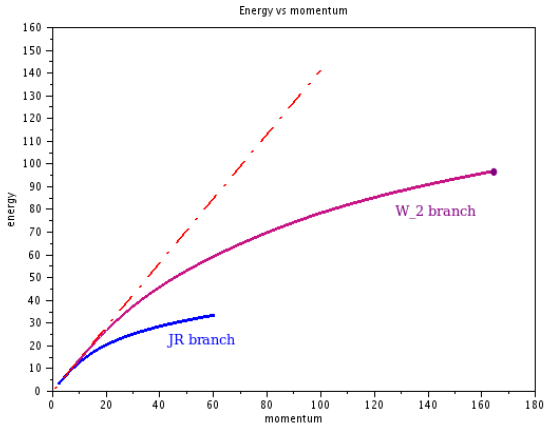

FIGURE 20. Energy-Momentum diagram with the JR branch (blue) and the new branch associated with the second Lump $\mathcal{W}_2$ (purple).

to $\mathcal{W}_2$ and $\mathcal{W}_3$ is that there is no solution to the nonlinear system (6), that is no critical point to the Kirchhoff action $\mathscr{F}$, with the symmetries we have imposed and six or ten (or even four) vortices.

5. VORTEX BRANCHES

As motivated in subsection 1.4, we wonder whether $(+2,-2)$ and $(+3,-3)$ vortex configuration would generate a new branch of travelling waves solutions to GP or even connect to the branches obtained in the previous section. These configurations can be designed and used as initializations in our algorithm for $c \approx 0$.

5.1. **Approximating the vortices**

The strategy adopted in this work consists in first finding a Padé approximant for the vortex profile of degree n, $\mathfrak{a}_n$ (see section 1.2 for notations), with here $n \in \{1,2,3\}$ from which one would create the "two vortices" configuration. A shooting method allows to compute an approximate numerical solution to (3) that will serve as a reference solution, denoted $\mathfrak{a}_n^{\text{ref}}$. For this problem, in order to avoid the singularities of the ODE (3) (the term $r \mapsto -n^2\mathfrak{a}_n/r^2$ in the ODE is the source of problems), it is convenient to implement the shooting method on the function $r \mapsto \mathfrak{a}_n(r)/r^n$. Indeed, from [24], we know that $y_n(r) \overset{\text{def}}{=} \mathfrak{a}_n(r)/r^n$ is an even power series of positive radius (thus the singularity is removed). Therefore, we apply the shooting method on the ODE for y_n given by: $y_n'' + (2n+1)y_n'/r = y_n(r^{2n}y_n^2 - 1)$, where we impose $y_n'(0) = 0$ and the shooting parameter is simply $y_n(0)$. For $n = 1$, we obtain $y_1(0) = \mathfrak{a}_1^{\text{ref}\,\prime}(0) \approx 0.58318949586$, which is slightly different from the value ≈ 0.5827811878 in [3].

Here we envisage two strategies for computing the Padé approximants. The first one is taken from [3] and consists in looking for a Padé of the form

$$\mathfrak{a}_1^{\text{Padé}}(r) \overset{\text{def}}{=} r\sqrt{\frac{a_0 + a_1 r^2}{1 + b_1 r^2 + b_2 r^4}}. \tag{29}$$

Since $\mathfrak{a}_1(r) \to 1$ for $r \to +\infty$, it is natural to set $b_2 = a_1$. To determine the other coefficients, we substitute $\mathfrak{a}_1^{\text{Padé}}$ in the equation (3) and Taylor expand the residual for $r \to 0$. We obtain three algebraic equations by cancelling the first coefficients of this Taylor expansion, and solve this system. We will refer to this method as

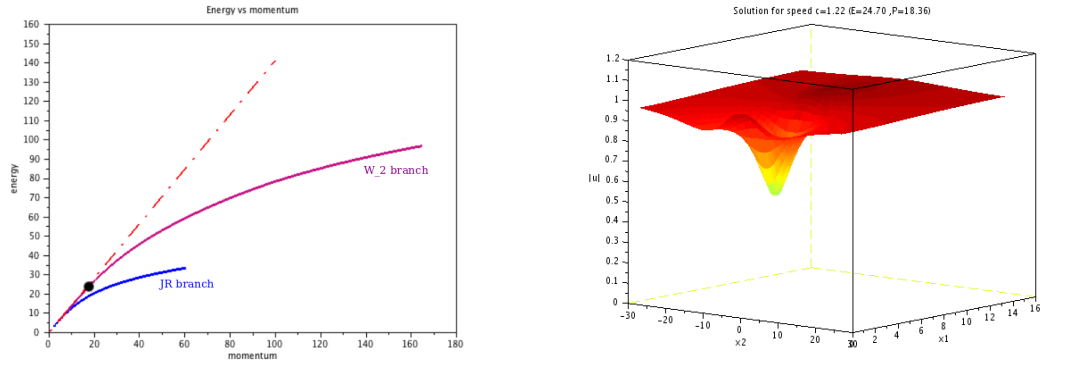

(A)

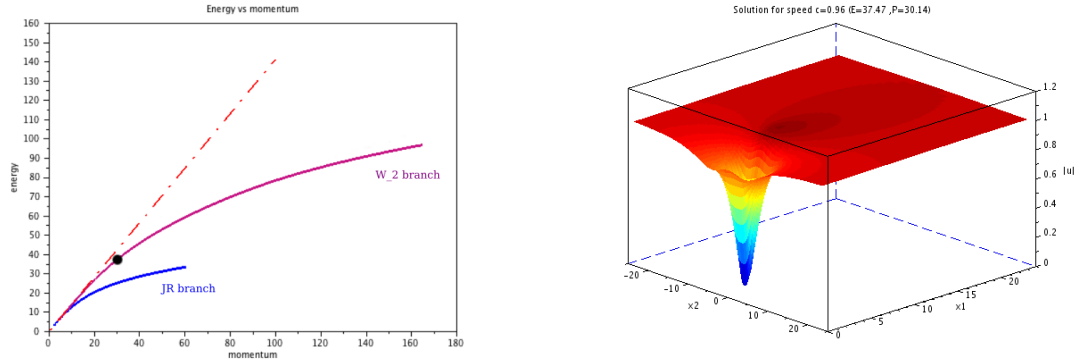

(B)

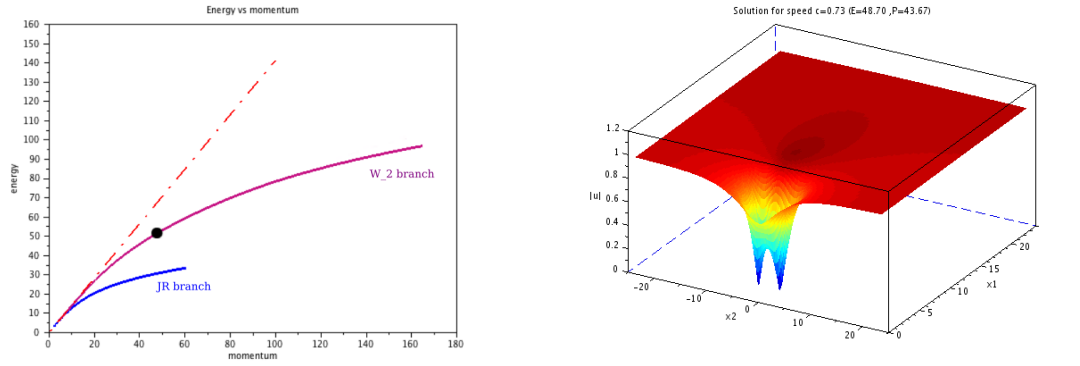

(C)

FIGURE 21. Travelling wave solution of the branch associated with the second Lump $\mathcal{W}_2$ for speeds: (A) $c = 1.22$; (B) $c = 0.96$; (C) $c = 0.73$. On the left-hand side, position in the Energy-Momentum diagram (spotted with a black point); on the right-hand side, modulus.

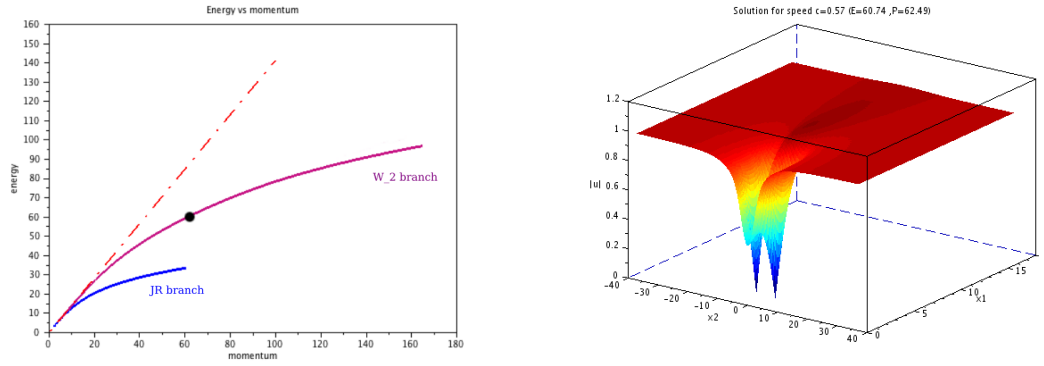

(A)

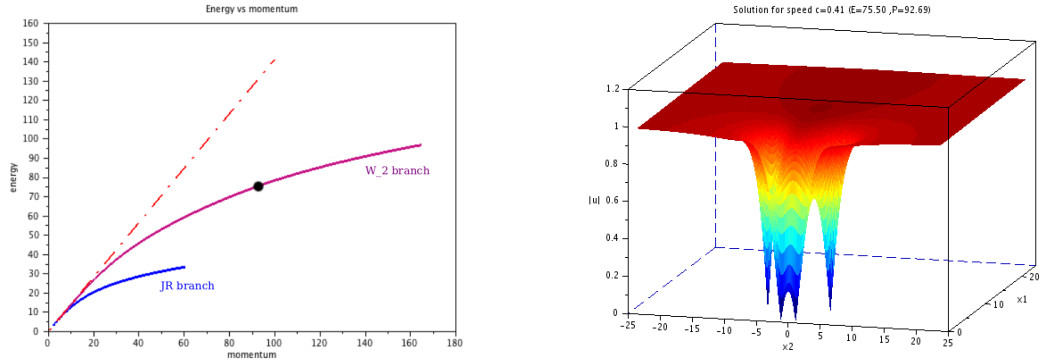

(B)

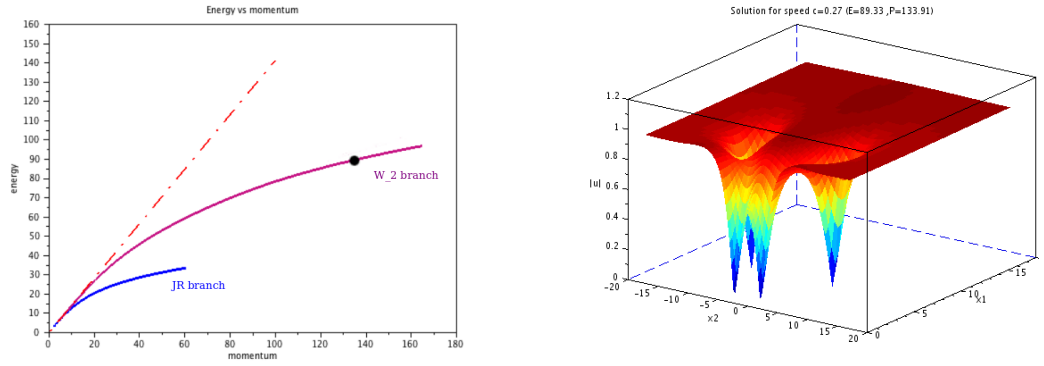

(C)

FIGURE 22. Travelling wave solution of the branch associated with the second Lump $\mathcal{W}_2$ for speeds: (A) $c = 0.57$; (B) $c = 0.41$; (C) $c = 0.27$. On the left-hand side, position in the Energy-Momentum diagram (spotted with a black point); on the right-hand side, modulus.

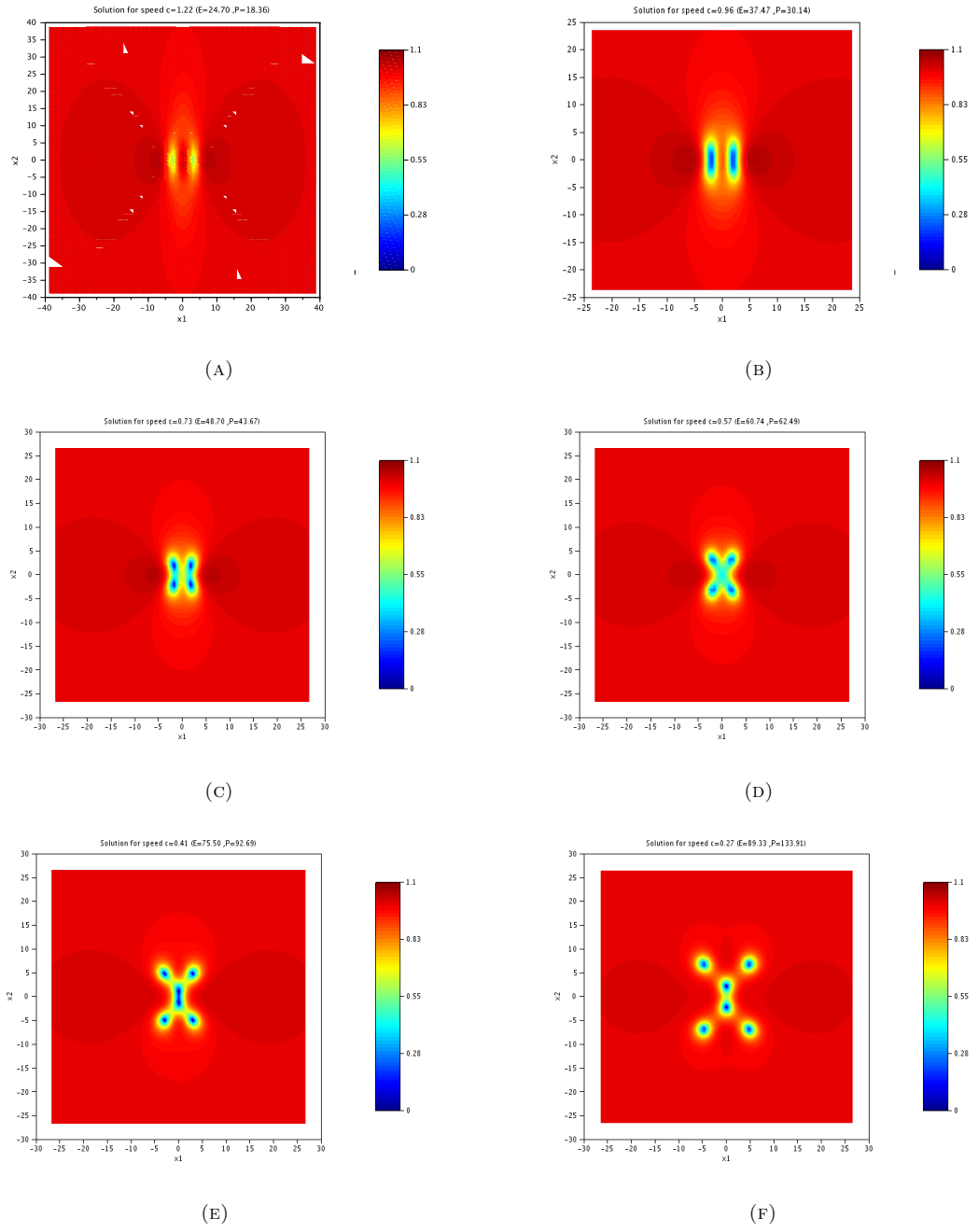

(A) (B)

(C) (D)

(E) (F)

FIGURE 23. Contourplots of the travelling waves of the branch associated with the $\mathcal{W}_2$ Lump: (A) $c = 1.22$; (B) $c = 0.96$; (C) $c = 0.73$; (D) $c = 0.57$; (E) $c = 0.411$; (F) $c = 0.27$.

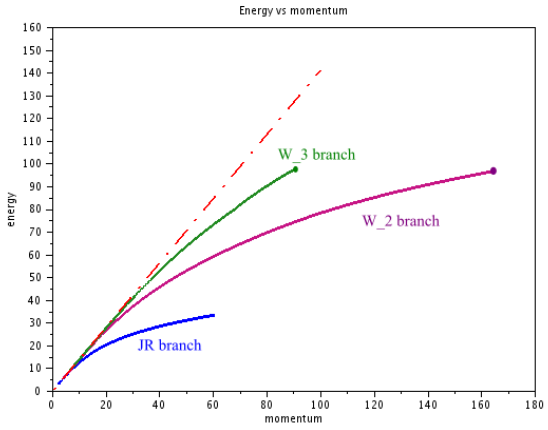

FIGURE 24. Energy-Momentum diagram with the JR branch (blue), the branch associated with the second lump $\mathcal{W}_2$ (purple) and with the third Lump $\mathcal{W}_3$ (green).

	Berloff's	*Least square*
L^2 error	0.0250530	0.0028370
L^∞ error	0.0097847	0.0013490

TABLE 3. Vortex of degree 1: L^2 and L^∞ errors between the Padé approximants and the numerical solution obtained with the shooting method.

Berloff's method, and this gives

$$\mathfrak{a}_1^{\mathrm{Be}}(r) \overset{\mathrm{def}}{=} r\sqrt{\frac{\frac{11}{32}+\frac{11}{384}r^2}{1+\frac{1}{3}r^2+\frac{11}{384}r^4}} = r\sqrt{\frac{0.3437+0.0286r^2}{1+0.3333r^2+0.0286r^4}}. \tag{30}$$

The advantage of this method is that we do not need to solve numerically the ODE (3) by a shooting method. The second method, referred to as the *least square method*, consist in fitting a Padé approximant to the numerical data given by the numerical solution $\mathfrak{a}_1^{\mathrm{ref}}$ obtained by the shooting method. In order to do so, we use a least square method and obtain

$$\mathfrak{a}_1^{\mathrm{ls}}(r) \overset{\mathrm{def}}{=} r\sqrt{\frac{0.3350601+0.0494196r^2}{1+0.3725704r^2+0.0494196r^4}}. \tag{31}$$

We may notice that $\mathfrak{a}_1(r)/r \to 0.58318949586$ when $r \to 0$. This has to be compared with $\sqrt{11/32} \approx 0.5863020$ and $\sqrt{0.3350601} \approx 0.5788438$. We may also compute the L^2 and L^∞ errors between $\mathfrak{a}_1^{\mathrm{Be}}$ (resp. $\mathfrak{a}_1^{\mathrm{ls}}$) and $\mathfrak{a}_1^{\mathrm{ref}}$ (see table 3). On figure 29, we see that $\mathfrak{a}_1^{\mathrm{Be}}$ gives a very good approximation, and that $\mathfrak{a}_1^{\mathrm{ls}}$ provides an excellent approximation.

We now focus on the degrees 2 and 3 that have not yet been addressed.

5.1.1. *Vortex of degree 2*

The solution obtained by the shooting method gives the approximate limit $r^{-2}\mathfrak{a}_2^{\mathrm{ref}}(r) \to 0.153099102859$ when $r \to 0$. In [3], the coefficients of the Padé approximant have been computed (with *Berloff's method*) and

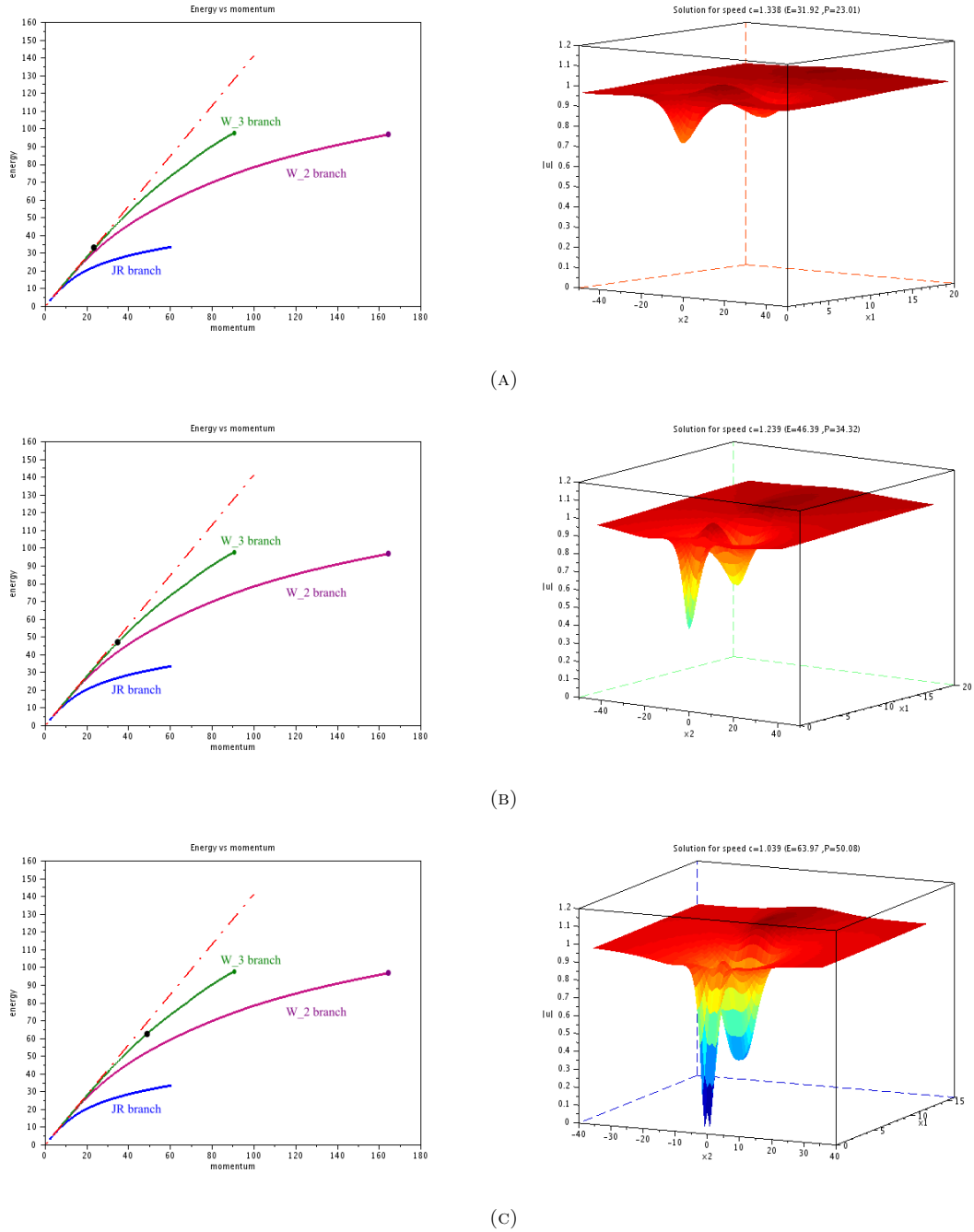

FIGURE 25. Travelling wave solution of the branch associated with the third Lump $\mathcal{W}_3$ for speeds: (A) $c = 1.34$; (B) $c = 1.24$; (C) $c = 1.04$. On the left-hand side, position in the Energy-Momentum diagram (spotted with a black point); on the right-hand side, modulus.

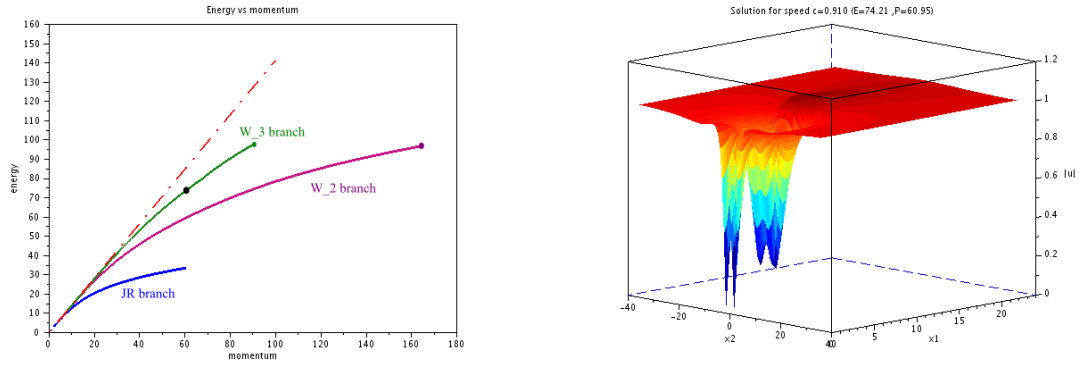

(A)

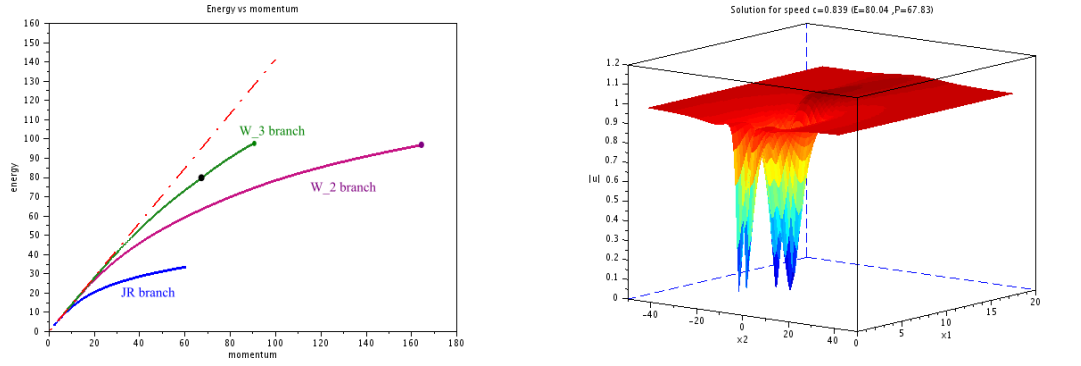

(B)

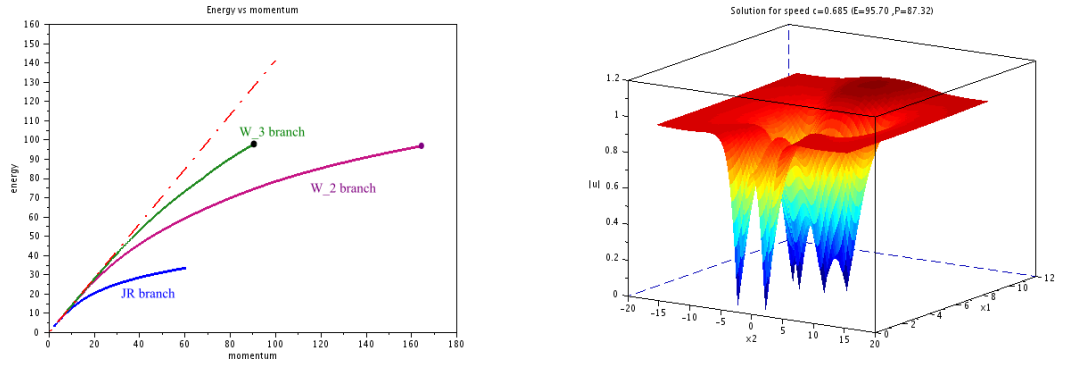

(C)

FIGURE 26. Travelling wave solution of the branch associated with the third Lump $\mathcal{W}_3$ for speeds: (A) $c = 0.91$; (B) $c = 0.84$; (C) $c = 0.685$. On the left-hand side, position in the Energy-Momentum diagram (spotted with a black point); on the right-hand side, modulus.

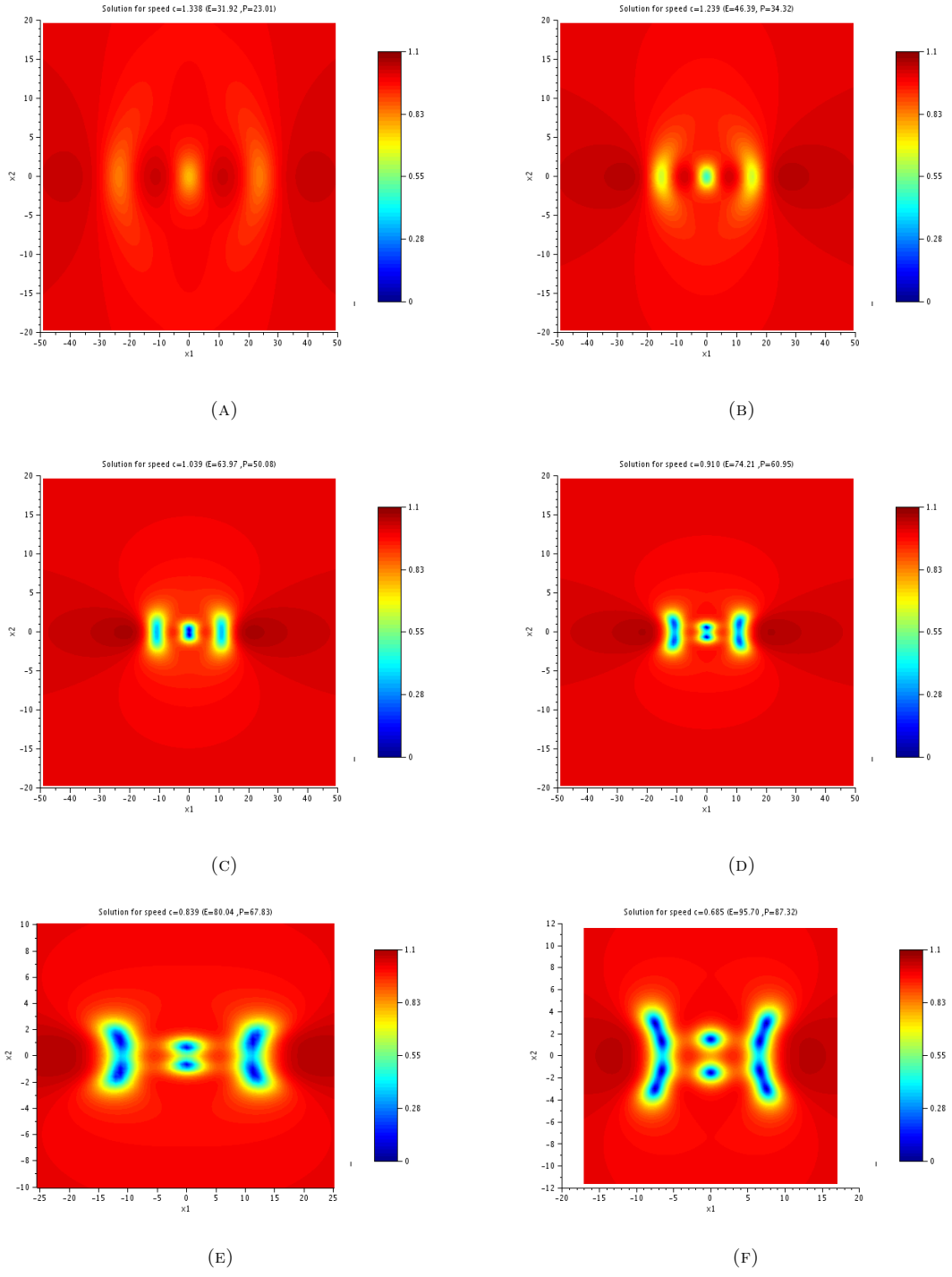

(A) (B)

(C) (D)

(E) (F)

FIGURE 27. Contourplots of the travelling waves of the branch associated with the $\mathcal{W}_3$ Lump: (A) $c = 1.34$; (B) $c = 1.24$; (C) $c = 1.04$; (D) $c = 0.91$; (E) $c = 0.84$; (F) $c = 0.685$.

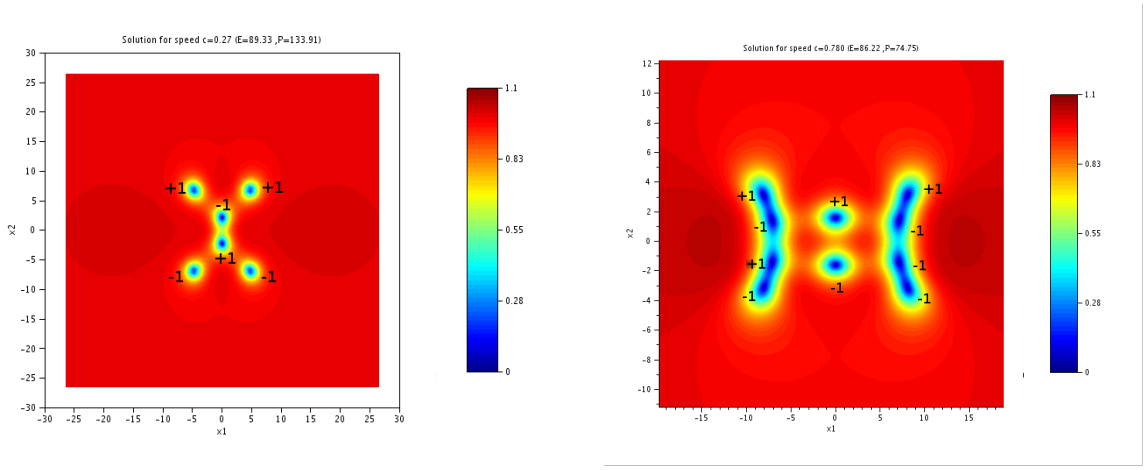

FIGURE 28. The charges of the vortices for the endpoint solution of the (A) $\mathcal{W}_2$-branch for $c = 0.27$; (B) $\mathcal{W}_3$-branch for $c = 0.780$.

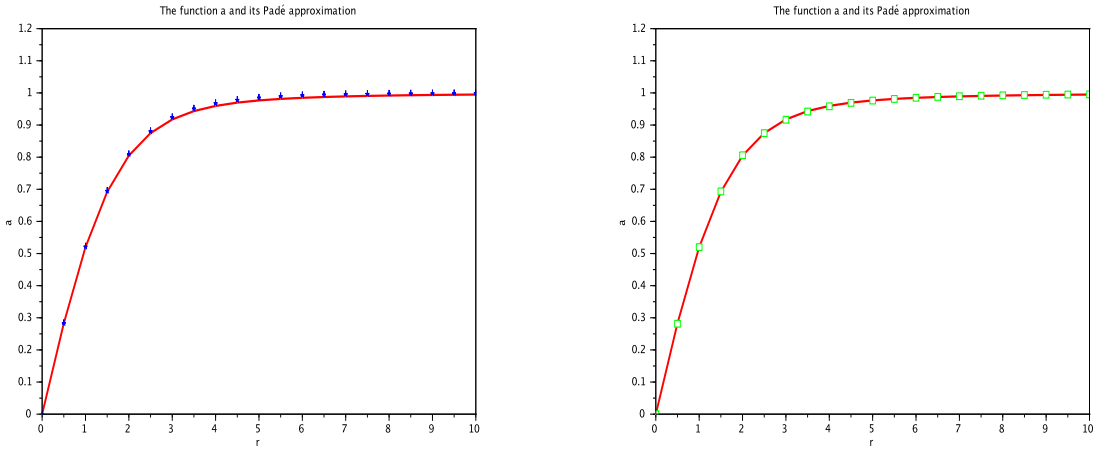

FIGURE 29. Profile of the degree 1 vortex $\mathfrak{a}_1$ (continuous red line) and Padé approximants: $\mathfrak{a}_1^{\mathrm{Be}}$ (30) in blue stars (left) and $\mathfrak{a}_1^{\mathrm{ls}}$ (31) in green squares (right)

give the expression

$$\mathfrak{a}_2^{\mathrm{Be}}(r) \stackrel{\mathrm{def}}{=} r^2\sqrt{\frac{0.02564396012 + 0.000626418393r^2}{1 + 0.1910941884r^2 + 0.01969625361r^4 + 0.000626418393r^6}} \tag{32}$$

that yields $r^{-2}\mathfrak{a}_2^{\mathrm{Be}}(r) \to \sqrt{0.02564396012} \approx 0.160137316$. Using the *least square method*, we obtain

$$\mathfrak{a}_2^{\mathrm{ls}}(r) \stackrel{\mathrm{def}}{=} r^2\sqrt{\frac{0.0208654 + 0.0010475r^2}{1 + 0.1504765r^2 + 0.0243630r^4 + 0.0010475r^6}}, \tag{33}$$

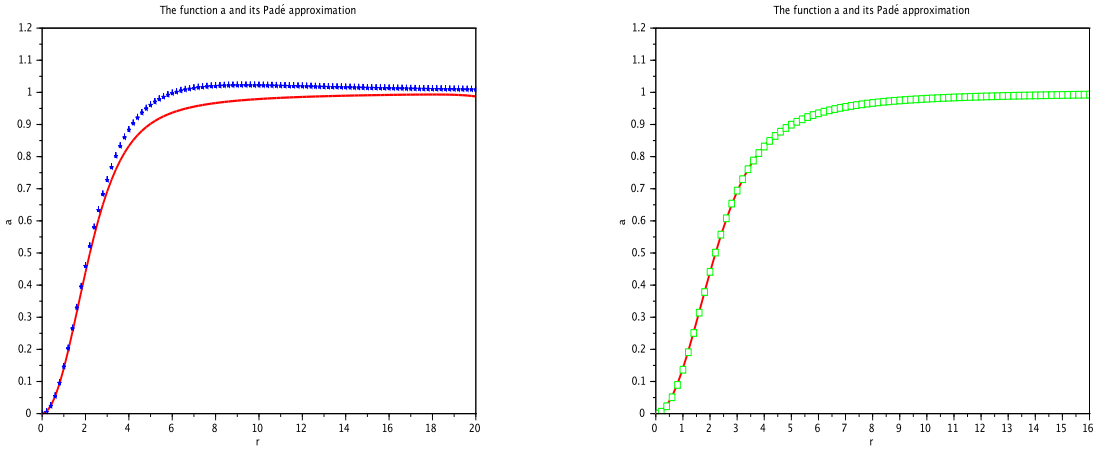

FIGURE 30. Profile of the degree 2 vortex $\mathfrak{a}_2^{\mathrm{ref}}$ (continuous red line) and Padé approximants: $\mathfrak{a}_2^{\mathrm{Be}}$ (32) in blue stars (left); $\mathfrak{a}_2^{\mathrm{ls}}$ (33) in green squares (right)

	Berloff's	*Least square*
L^2 error	0.1721167	0.0066131
L^∞ error	0.0619714	0.0084585

TABLE 4. Vortex of degree 2: L^2 and L^∞ errors between the Padé approximants and the numerical solution obtained with the shooting method.

that gives the asymptotic $r^{-2}\mathfrak{a}_2^{\mathrm{ls}}(r) \to \sqrt{0.0208654} \approx 0.1444486$. In figure 30, we plot $\mathfrak{a}_2^{\mathrm{ref}}$, $\mathfrak{a}_2^{\mathrm{Be}}$, $\mathfrak{a}_2^{\mathrm{ls}}$. We also measure the L^2 and L^∞ errors between $\mathfrak{a}_2^{\mathrm{Be}}$ (resp. $\mathfrak{a}_2^{\mathrm{ls}}$) and $\mathfrak{a}_2^{\mathrm{ref}}$ (see table 4). We notice a much better fit if one uses the least square method. Notice for instance that $\mathfrak{a}_2^{\mathrm{Be}}$ reaches values larger than 1.

In order to improve the quality of the Padé approximation, one could imagine to consider a higher degree Padé approximant, namely, for our problem, replacing in the square root the rational function by the quotient of a polynomial of degree 4 by a polynomial of degree 8. With *Berloff's method*, we obtain the following expression for the Padé approximant of the vortex of degree 2 :

$$\mathfrak{a}_{2bis}^{\mathrm{Be}}(r) \stackrel{\mathrm{def}}{=} r^2\sqrt{\frac{0.0235754388705356 + 0.001903033787r^2 + 0.00007439596524r^4}{1 + 0.2473877000r^2 + 0.03223416114r^4 + 0.002100897817r^6 + 0.00007439596524r^8}} \tag{34}$$

and with the *least square method*

$$\mathfrak{a}_{2bis}^{\mathrm{ls}}(r) \stackrel{\mathrm{def}}{=} r^2\sqrt{\frac{0.02247580 - 0.0016723r^2 + 0.0002102r^4}{1 + 0.0477937r^2 + 0.0242546r^4 - 0.0008577r^6 + 0.0002102r^8}} \tag{35}$$

with the corresponding plots (see figure 31) and the errors given in table 5. Comparing with $\mathfrak{a}_2^{\mathrm{Be}}$, it is noticeable that the L^2 error is almost the same and the L^∞ error is multiplied by 2. If we compare $\mathfrak{a}_2^{\mathrm{ls}}$ with $\mathfrak{a}_{2bis}^{\mathrm{ls}}$, we may notice that the errors are not significantly improved.

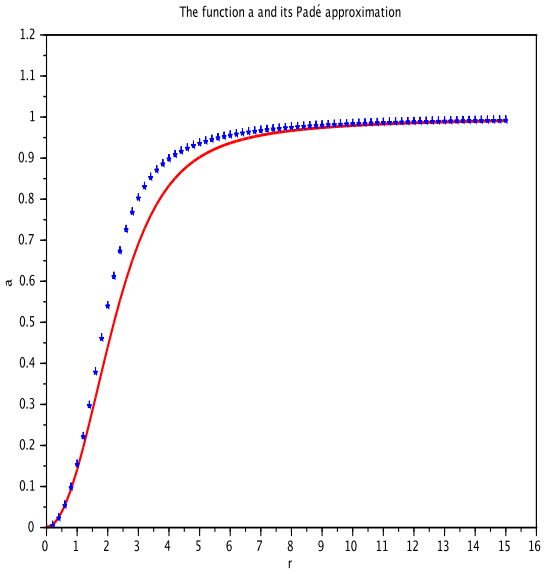

FIGURE 31. Profile of the degree 2 vortex $\mathfrak{a}_2^{\text{ref}}$ (continuous red line) and the Padé approximant of higher degree $\mathfrak{a}_{2bis}^{\text{Be}}$ (32) (blue stars).

	Berloff's	*least square*
L^2 error	0.1721125	0.0040721
L^∞ error	0.1225094	0.0079088

TABLE 5. Vortex of degree 2 and Padé approximants of higher degree: L^2 and L^∞ errors with the numerical solution obtained with the shooting method.

5.1.2. *Vortex of degree 3*

We explore the case of the degree 3 vortex in an analogous way. The approximate asymptotic given by the numerical solution obtained by the shooting method reads now $\mathfrak{a}_3^{\text{ref}}(r)/r^3 \to 0.026183420716$ when $r \to 0$, *Berloff's method* gives $\mathfrak{a}_3^{\text{Be}}(r)/r^3 \to \sqrt{0.0007951684094} \approx 0.028198731$ and the expression

$$\mathfrak{a}_3^{\text{Be}}(r) \stackrel{\text{def}}{=} r^3 \sqrt{\frac{0.0007951684094 + 0.00000864664692r^2}{1 + 0.1358739820r^2 + 0.009952997746r^4 + 0.0005274760603r^6 + 0.00000864664692r^8}}. \tag{36}$$

The *least square method* gives $\mathfrak{a}_3^{\text{ls}}(r)/r^3 \to \sqrt{0.0007568} \approx 0.0275100$ and

$$\mathfrak{a}_3^{\text{ls}}(r) \stackrel{\text{def}}{=} r^3 \sqrt{\frac{0.0007568 + 0.0000041r^2}{1 + 0.1846304r^2 + 0.0050719r^4 + 0.0008052r^6 + 0.0000041r^8}} \tag{37}$$

We plot these approximations in figure 32 and the errors in table 6. Same remarks as for the degree 2 vortex hold.

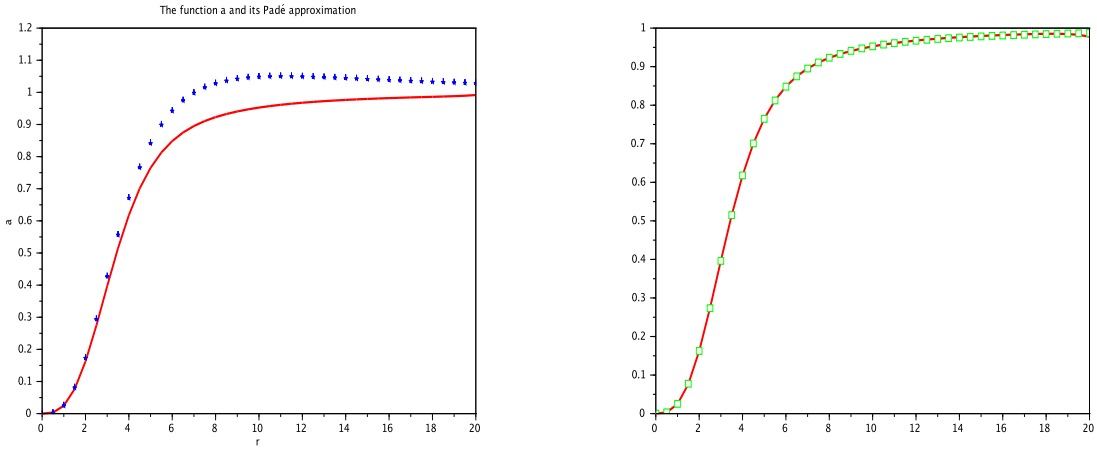

FIGURE 32. Profile of the degree 3 vortex $\mathfrak{a}_3$ and Padé approximants: $\mathfrak{a}_3^{\mathrm{Be}}$ (36) in blue stars (left); $\mathfrak{a}_3^{\mathrm{ls}}$ (37) in green squares (right)

	Berloff's	*Least square*
L^2 error	0.3215535	0.0062027
L^∞ error	0.1063004	0.0094989

TABLE 6. vortex of degree 3: L^2 and L^∞ errors with the numerical solution obtained with the shooting method.

5.1.3. *Two vortices configurations*

The travelling vortex solution with small speed that we would like to use consists in two vortices of degrees $+n$ and $-n$ at large distance from each other (in a similar way as in the degree one case, see [15] for details). A good approximation of this solution for c small would be given by

$$u^{\mathrm{app}}_{\pm n\,\mathrm{vortices}}(x_1,x_2)=\mathfrak{a}_n(|(x_1,x_2-c^{-1})|)\left(\frac{x_1+i(x_2-c^{-1})}{|(x_1,x_2-c^{-1})|}\right)^n\times\mathfrak{a}_n(|(x_1,x_2+c^{-1})|)\left(\frac{x_1-i(x_2+c^{-1})}{|(x_1,x_2+c^{-1})|}\right)^n. \quad (38)$$

We use this expression in order to initialize our continuation algorithm with small speeds.

5.2. $(+2,-2)$ vortex configuration

The $(+2,-2)$ configuration depicted in Figure 33 is obtained by using (38) and the Padé approximant defined in the previous section with the least square method. It is not a travelling wave solution for GP, but has nevertheless allowed us to achieve a numerical solution. Let us mention that the relative residual obtained with the least square Padé approximant is better than Berloff's.

We obtain a new branch of travelling wave solutions using our algorithm, which are represented in figure 34. It is remarkable that as the speed increases the ± 2 vortices split into two ± 1 vortices. The distance between two $+1$ vortices (resp. two -1 vortices) is significantly smaller than the distance between vortices of degree $+1$ and -1. As for the $\mathcal{W}_2$ and the $\mathcal{W}_3$ branches, our numerical methods no longer converge for $c > 0.386$. These solutions are clearly qualitatively different from those on the branches obtained in section 4. The complete

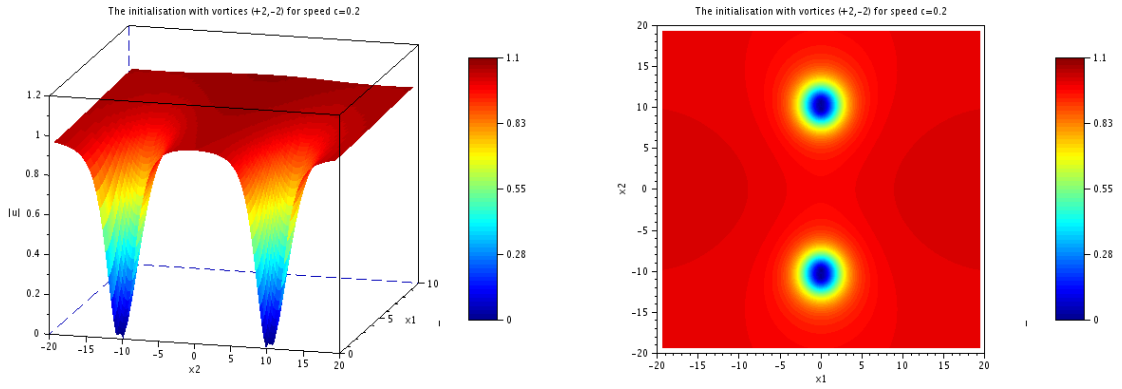

FIGURE 33. Initialization for the $(+2,-2)$ configuration. Modulus on the left and contourplot on the right.

Energy-Momentum diagram augmented with the $(+2,-2)$ branch (in black) is plotted on Figure 35.

5.3. $(+3,-3)$ vortex configuration

We depict the $(+3,-3)$ configuration for two different speeds in Figures 36 and 37. This time, the initial vortex of degree three splits into three vortices of degree one, in a same way as in the previous subsection. We have then obtained all the branches of the Energy-Momentum diagram of Figure 2. Here again, our numerical methods no longer converge for $c > 0.507$. In figure 37 (B), we see two rather large regions in the half-plane $\{x_1 > 0\}$, near the points $(3,+6)$ and $(3,-6)$, where the wave function has small modulus. In view of the evolution as c increases, we can think that each of these regions contains exactly one zero of the travelling wave, respectively of charge $+1$ and -1, and one point of local minimum for the modulus.

6. CONCLUSION

We have investigated the existence of travelling waves for the two dimensional GP equation. Besides the well-known Jones-Roberts branch, our numerical approach shows the existence of at least four other branches of travelling waves. Two of them are related to the KP-I limit $c \to \mathfrak{c}_s$ through the existence (see [32]) of explicit solitary waves for KP-I different from the Lump (the latter being probably the ground state). The last two branches are associated with critical points of the Kirchhoff action involving vortices of degree larger than one. Furthermore, we also took advantage of the fact that the solitary waves exhibited in [32] belong to a family of lumps solitary waves to KP-I with free parameters and study their spectral properties. The study of their persistence as travelling waves to GP (as we did in this paper for the solutions exhibited in [32]) is a very interesting question, beyond the scope of this work, especially because the degeneracy (that we managed to kill in this work by using symmetries) will be a delicate issue to solve. This will be the subject of further investigation.

In a future work, we also wish to investigate the dynamical stability issues concerning these travelling waves. The travelling waves on the Jones-Roberts branch are orbitally stable (see [14]), and this is related to the concavity of the curve $P \mapsto E$ combined with the fact that the Hessian of the action $d^2(E - cP)$ has exactly one negative eigenvalue. The situation is actually not very clear for our new branches since there are presumably many negative eigenvalues. We also hope to be able to give some rigorous existence results for these branches.

We are convinced that these new branches also exist in space dimension three, in an axisymmetric setting. For the JR branch, the three dimensional case has already been studied in [25] (see [6, 8, 11, 14, 30] for rigorous

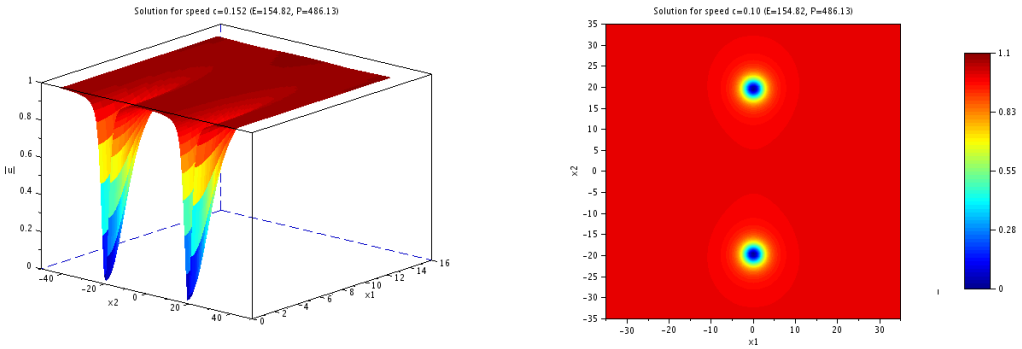

(A)

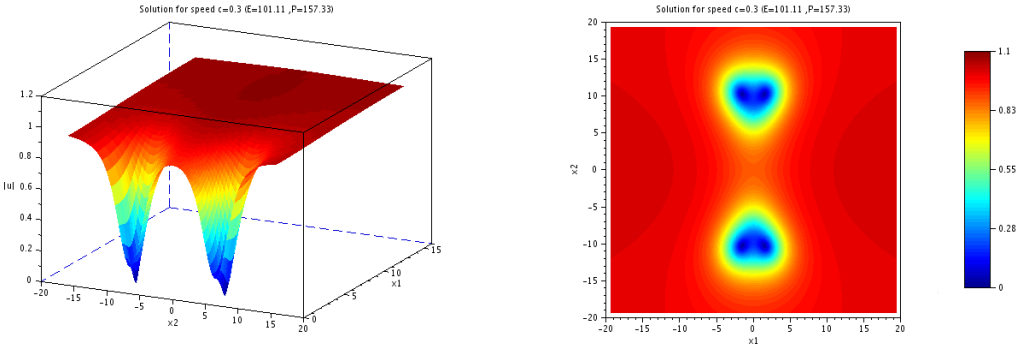

(B)

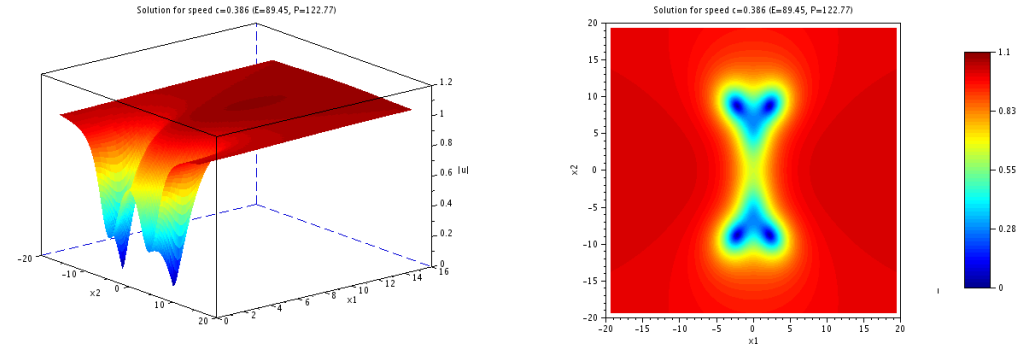

(C)

FIGURE 34. Travelling wave associated with the $(+2,-2)$ configuration for speeds: (A) $c = 0.1$; (B) $c = 0.3$; (C) $c = 0.386$. On the left-hand side modulus; on the right-hand side contourplot.

mathematical results). In the vortex limit $c \to 0$, the travelling wave is a vortex ring of large radius. The three dimensional analogue of our branch with $(+2,-2)$ or $(+3,-3)$ vortices would then be travelling waves with two or three parallel vortex rings at small distance one from another. This should probably be related to travelling vortex knots in Bose condensates as studied in [35] when the poloidal radius is rather small.

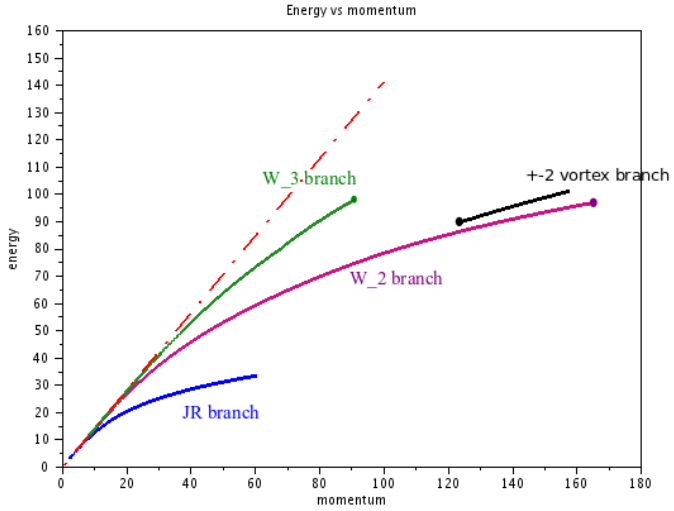

FIGURE 35. Energy-Momentum diagram with the additional branch (in black) associated with the $(+2, -2)$ vortex configuration.

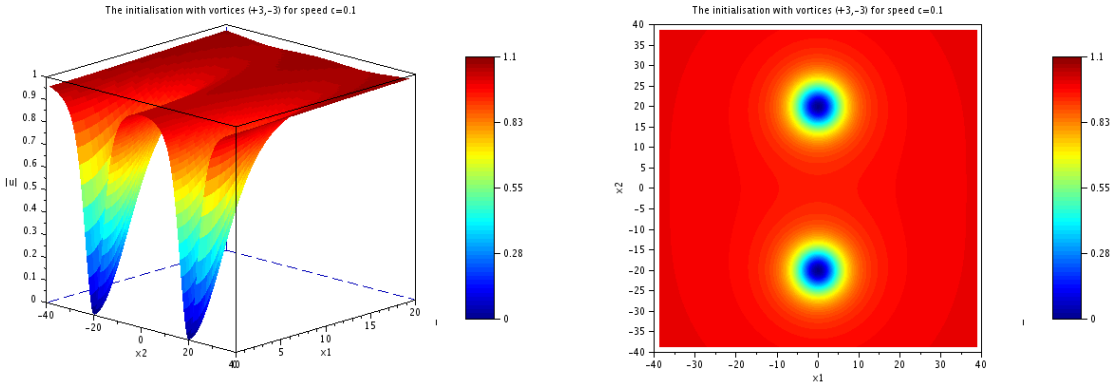

FIGURE 36. Initialization for the $(+3, -3)$ configuration. Modulus on the left and contourplot on the right.

Acknowledgements: This work is supported by the ANR project *BoND* (Bond-ANR-13-BS01-0009-02). We would like to thank Fabrice Béthuel for having raised to D.C. the question of existence of travelling waves to GP with vortices of degree higher than one. At that time, we were looking for solutions with two vortices, one of degree $+2$ and one of degree -2. We finally would like to thank the anonymous referees for their very relevant questions and comments that helped to improve this paper through the section 3.3.

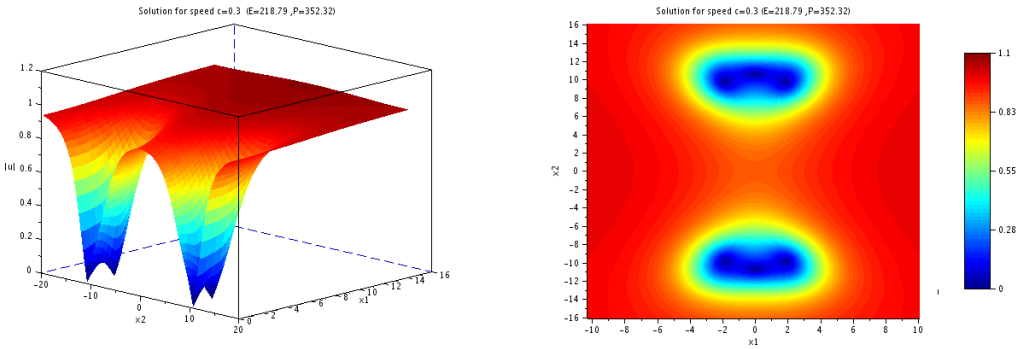

(A)

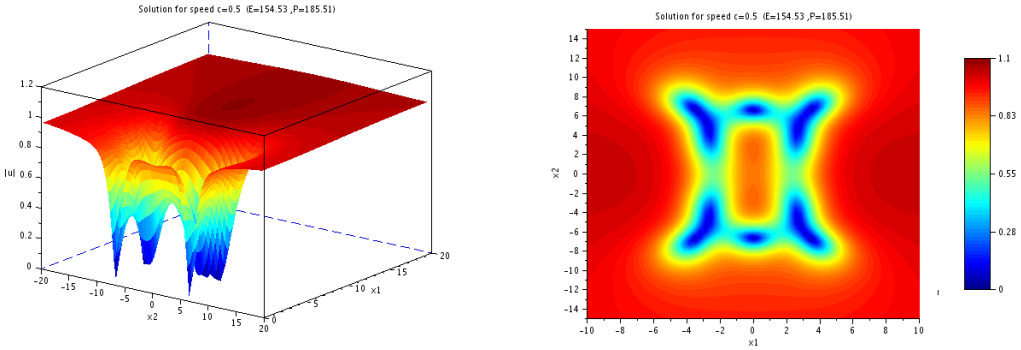

(B)

FIGURE 37. Travelling wave associated with the $(+3,-3)$ configuration for speeds: (A) $c=0.3$; (B) $c=0.507$. On the left-hand side modulus; on the right-hand side contourplot.

APPENDIX A. ON THE DERIVATION OF THE FORMULAS (27) AND (28)

As in [32], we apply the Hirota method and look for a solution to

$$\partial_{z_1}\mathcal{W}-\partial_{z_1}^3\mathcal{W}+\mathcal{W}\partial_{z_1}\mathcal{W}+\partial_{z_2}^2\partial_{z_1}^{-1}\mathcal{W}=0 \tag{SW}$$

under the form $\mathcal{W}=-12\partial_1^2\ln\phi$. This puts (SW) in bilinear form:

$$\phi(\partial_{z_1}^2\phi+\partial_{z_2}^2\phi-\partial_{z_1}^4\phi)=(\partial_{z_1}\phi)^2+(\partial_{z_2}\phi)^2+3(\partial_{z_1}^2\phi)^2-4\partial_{z_1}\phi\partial_{z_1}^3\phi. \tag{39}$$

We look for polynomial solutions ϕ to (39). If ϕ has degree d, then, in (39), $\phi\Delta\phi$ and $(\partial_{z_1}\phi)^2+(\partial_{z_2}\phi)^2$ have degree $\leqslant 2d-2$ whereas $\phi\partial_{z_1}^4\phi$ and $3(\partial_{z_1}^2\phi)^2-4\partial_{z_1}\phi\partial_{z_1}^3\phi$ have degree $\leqslant 2d-4$. We decompose $\phi=\sum_{j=0}^d\dot\phi_j$, where $\dot\phi_j$ is homogeneous of degree j, insert this into (39) and cancel out the terms of homogeneous degree $2d-2$ to 0 one by one. By considering the terms of homogeneous degree $2d-2$, we obtain the equation for $\dot\phi_d$:

$$\dot\phi_d\Delta\dot\phi_d=(\partial_{z_1}\dot\phi_d)^2+(\partial_{z_2}\dot\phi_d)^2. \tag{40}$$

It turns out that for even d, $(z_1^2+z_2^2)^{d/2}$ is a solution to (40). Actually, one can check that the only homogeneous solutions to (40) of degree d are multiples of $(z_1^2+z_2^2)^{d/2}$. The lump solitary waves $\mathcal{W}_2$ and $\mathcal{W}_3$ we are interested

in correspond to the cases $d = 6$ and $d = 12$ (and more generally, as mentioned in [32], the case $d = m(m+1)$ for m a positive integer). When j decreases from $d-1$ to 0, since the equation is polynomial in ϕ and its derivatives, we obtain linear equations of the form

$$\begin{aligned}&\dot\phi_d\Delta\dot\phi_j + \dot\phi_j\Delta\dot\phi_d - 2\partial_{z_1}\dot\phi_d\partial_{z_1}\dot\phi_j - 2\partial_{z_2}\dot\phi_d\partial_{z_2}\dot\phi_j\\ &= (z_1^2+z_2^2)^{d/2-1}\Big[(z_1^2+z_2^2)\Delta\dot\phi_j + d^2\dot\phi_j - 2d(z_1\partial_{z_1}+z_2\partial_{z_2})\dot\phi_j\Big] = \dot S_j,\end{aligned} \tag{41}$$

where the source term $\dot S_j$ depends on $\dot\phi_d, \dots, \dot\phi_{j+1}$ and contains only the terms of degree $d-2+j$ of the complete source term S_j (including the contributions of $\dot\phi_d, \dots, \dot\phi_{j+1}$). When we solve this equation, it may happen that there is a nontrivial kernel, which produces free parameters. Moreover, we have to impose that the source term belongs to the image of the operator on the left-hand side (in particular, it has to be factorizable by $(z_1^2+z_2^2)^{d/2-1}$), which produces some constraints on the free parameters.

For instance, for $d = 6$, we obtain $S_5 = 144z_1^6z_2^2 - 72z_1^4z_2^4 + 144z_1^2z_2^6 + 180z_1^8 + 180z_2^8 = 36(z_1^2+z_2^2)^2(5z_1^4 - 6z_1^2z_2^2 + 5z_2^4)$, $\dot S_5 = 0$, and $\dot\phi_5 = \tau_1(z_1^5 + z_1^4z_2 + 2z_1^3z_2^2 + 2z_1^2z_2^3 + z_1z_2^4 + z_2^5) + \tau_2(z_1^4z_2 + 2z_1^2z_2^3 + z_2^5)$ for some parameters τ_1, $\tau_2 \in \mathbb{R}$. This kernel was expected since the two space derivatives $\partial_1\dot\phi_6$ and $\partial_2\dot\phi_6$ are linearly independent solutions to the homogeneous equation (41). In the following, we shall remove the invariance by translation by imposing $\tau_1 = \tau_2 = 0$. Then, we obtain $S_4 = \dot S_4 = S_5 = 36(z_1^2+z_2^2)^2(5z_1^4 - 6z_1^2z_2^2 + 5z_2^4)$ and $\dot\phi_4 = \alpha_4z_1^4 + \alpha_3z_1^3z_2 + 90z_1^2z_2^2 + \alpha_3z_1z_2^3 + (42-\alpha_4)z_2^4$ for some constants α_3, α_4. Then, for $j = 3$, we obtain $\dot S_3 = 0$ and $\dot\phi_3 = \alpha_1z_1^3 - 3\alpha_2z_1^2z_2 - 3\alpha_1z_1z_2^2 + \alpha_2z_2^3$ for some parameters α_1, α_2. When $j = 2$, we obtain $-\dot S_2 = -4\alpha_4^2z_1^6 + 132z_1^6\alpha_4 - \alpha_3^2z_1^6 - 36\alpha_3z_1^5z_2 - 108\alpha_4z_1^4z_2^2 - 12\alpha_4^2z_1^4z_2^2 - 3\alpha_3^2z_1^4z_2^2 + 5400z_1^4z_2^2 - 648\alpha_3z_1^3z_2^3 - 32400z_1^2z_2^4 + 1116\alpha_4z_1^2z_2^4 - 3\alpha_3^2z_1^2z_2^4 - 12\alpha_4^2z_2^4z_1^2 - 36\alpha_3z_1z_2^5 - 9000z_2^6 + 204\alpha_4z_2^6 - 4\alpha_4^2z_2^6 - \alpha_3^2z_2^6$. It turns out that $\dot S_2$ is not factorizable by $(z_1^2+z_2)^2$ unless $(\alpha_3,\alpha_4) = (0,25)$. Under this constraint, we obtain $\dot S_2 = -800(z_1^2+z_2^2)^2(z_1^2-8z_2^2)$ and $\dot\phi_2 = -125z_1^2 + 475z_2^2$. For $j = 1$, we have $\dot S_1 = -24(z_1^2+z_2^2)^2(\alpha_1z_1 + 5\alpha_2z_2)$ and $\dot\phi_1 = -\alpha_1z_1 - 5\alpha_2z_2$. Finally, $\dot S_0 = 9(z_1^2+z_2^2)^2(7500 + \alpha_1^2 + \alpha_2^2)$ and $\dot\phi_0 = \alpha_1^2/4 + \alpha_2^2/4 + 1875$, which gives $S_{-1} = 0$, that is we have a solution to (39).

The computations for $d = 12$ are similar.

In order to show that for any $\boldsymbol{\alpha} \in \mathbb{R}^2$ and $z \in \mathbb{R}^2$, we have $\phi_2^{\boldsymbol{\alpha}}(z) > 0$, we first write

$$\alpha_1z_1^3 - 3\alpha_1z_1z_2^2 - \alpha_1z_1 + \alpha_1^2/4 = (\alpha_1/2 + z_1^3 - 3z_1z_2^2 - z_1)^2 - z_1^6 + 6z_1^4z_2^2 - 9z_1^2z_2^4 + 2z_1^4 - 6z_1^2z_2^2 - z_1^2$$

and symmetrically, by exchanging the indices 1 and 2 to infer

$$\begin{aligned}\phi_2^{\boldsymbol{\alpha}}(z) &= (z_1^2+z_2^2)^3 + 27z_1^4 + 78z_1^2z_2^2 + 19z_2^4 + (\alpha_1/2 + z_1^3 - 3z_1z_2^2 - z_1)^2 + (\alpha_2/2 + z_2^3 - 3z_1^2z_2 - z_2)^2\\ &\quad - z_1^6 - z_2^6 - 3z_1^4z_2^2 - 3z_1^2z_2^4 - 126z_1^2 + 474z_2^2 + 1875\\ &= 27z_1^4 + 78z_1^2z_2^2 + 19z_2^4 + (\alpha_1/2 + z_1^3 - 3z_1z_2^2 - z_1)^2 + (\alpha_2/2 + z_2^3 - 3z_1^2z_2 - z_2)^2\\ &\quad - 126z_1^2 + 474z_2^2 + 1875.\end{aligned}$$

The result follows from the lower bound $27z_1^4 - 126z_1^2 \geqslant -147$.

References

[1] M. Abid, C. Huepe, S. Metens, C. Nore, C.T. Pham, L.S. Tuckerman, and M.E. Brachet. Gross-Pitaevskii dynamics of Bose-Einstein condensates and superfluid turbulence. *Fluid Dynamics Research*, 33(5-6):509–544, 2003.

[2] L. A. Abramyan and Yu. A. Stepanyants. Two-dimensional multisolitons: stationary solutions of the Kadomtsev-Petviashvili equation. *Radiophysics and Quantum Electronics*, 28:20–26, 1985.

[3] N. Berloff. Padé approximations of solitary wave solutions of the Gross-Pitaevskii equation. *J. Phys. A: Math. Gen.*, 37(5):1617–1632, 2004.

[4] F. Bethuel, H. Brezis, and F. Hélein. *Ginzburg-Landau vortices*. Progress in Nonlinear Differential Equations and their Applications, 13. Birkhäuser Boston, Inc., Boston, MA, 1994.

[5] F. Béthuel, P. Gravejat, and J-C. Saut. On the KP-I transonic limit of two-dimensional Gross-Pitaevskii travelling waves. *Dynamics of PDE*, 5(3):241–280, 2008.

[6] F. Béthuel, P. Gravejat, and J-C. Saut. Travelling waves for the Gross-Pitaevskii equation. II. *Comm. Math. Phys.*, 285(2):567–651, 2009.

[7] F. Béthuel, R. L. Jerrard, and D. Smets. On the NLS dynamics for infinite energy vortex configurations on the plane. *Rev. Mat. Iberoam.*, 24(2):671–702, 2008.

[8] F. Béthuel, G. Orlandi, and D. Smets. Vortex rings for the Gross-Pitaevskii equation. *J. Eur. Math. Soc. (JEMS)*, 6(1):17–94, 2004.

[9] F. Béthuel and J-C. Saut. Travelling waves for the Gross-Pitaevskii equation. I. *Ann. Inst. H. Poincaré Phys. Théor.*, 70(2):147–238, 1999.

[10] X. Chen, C. M. Elliott, and T. Qi. Shooting method for vortex solutions of a complex-valued Ginzburg-Landau equation. *Proceedings of the Royal Society of Edinburgh: Section A Mathematics*, 124:1075–1088, 1 1994.

[11] D. Chiron. Travelling waves for the Gross-Pitaevskii equation in dimension larger than two. *Nonlinear Anal., Theory, Methods, Appl.*, 58(1-2):175–204, 2004.

[12] D. Chiron. Travelling waves for the Nonlinear Schrödinger Equation with general nonlinearity in dimension one. *Nonlinearity*, 25:813–850, 2012.

[13] D. Chiron and M. Mariş. Rarefaction pulses for the Nonlinear Schrödinger Equation in the transonic limit. *Comm. Math. Phys.*, 326(2):329–392, 2014.

[14] D. Chiron and M. Mariş. Traveling Waves for Nonlinear Schrödinger Equations with Nonzero Conditions at Infinity. *Arch. Rational Mech. Anal.*, 226(1):143–242, 2017.

[15] D. Chiron and C. Scheid. Travelling waves for the Nonlinear Schrödinger Equation with general nonlinearity in dimension two. *Journal of Nonlinear Science*, 26(2):171–231, 2016.

[16] A. de Bouard and J.-C. Saut. Solitary waves of generalized Kadomtsev-Petviashvili equations. *Ann. Inst. H. Poincaré Anal. Non Linéaire*, 14(2):211–236, 1997.

[17] L. Di Menza. Numerical computation of solitons for optical systems. *M2AN Math. Model. Numer. Anal.*, 43(1):173–208, 2009.

[18] G. Doulis and J. Frauendiener. Global simulations of Minkowski spacetime including spacelike infinity. *Phys. Rev. D*, 95:024035, 2017.

[19] A. L. Fetter. Vortices in an imperfect Bose Gas. iv. Translational Velocity. *Phys. Rev.*, 151(1):100–104, 1966.

[20] V. M. Galkin, D. E. Pelinovsky, and Yu. A. Stepanyants. The structure of the rational solutions to the Boussinesq equation. *Physica D*, 80:246–255, 1995.

[21] V. L. Ginzburg and L. P. Pitaevskii. On the theory of superfluidity. *Sov. Phys. JETP*, 7(5):858–861, 1958.

[22] K. A. Gorshov, D. E. Pelinovsky, and Yu. A. Stepanyants. Normal and anomalous scattering, formation and decay of bound states of two dimensional solitons described by the Kadomtsev-Petviashvili equation. *JETF*, 77:237–245, 1993.

[23] P. Gravejat. First order asymptotics for the travelling waves in the Gross-Pitaevskii equation. *Adv. Differential Equations*, 11(3):259–280, 2006.

[24] R.-M. Hervé and M. Hervé. Étude qualitative des solutions réelles d'une équation différentielle liée à l'équation de Ginzburg-Landau. *Ann. Inst. H. Poincaré Anal. Non Linéaire*, 11(4):427–440, 1994.

[25] C. Jones and P. Roberts. Motion in a Bose condensate IV. Axisymmetric solitary waves. *J. Phys. A: Math. Gen.*, 15:2599–2619, 1982.

[26] Y. Kivshar and B. Luther-Davies. Dark optical solitons: physics and applications. *Physics Reports*, 298:81–197, 1998.

[27] H. Lamb. *Hydrodynamics*. Cambridge, UK. Cambridge Univ. Press. 6th ed, 1932.

[28] W. Liu and J. Wei. Nondegeneracy of the Lump Solution to the KP-I Equation. *Preprint*, 2017.

[29] S. Manakov, V. Zakharov, L. Bordag, A. Its, and V. Matveev. Two-dimensional solitons of the Kadomtsev-Petviashvili equation and their interaction. *Phys. Lett. A*, 63:205–206, 1977.

[30] M. Mariş. Traveling waves for nonlinear Schrödinger equations with nonzero conditions at infinity. *Ann. of Math.*, 178:107–182, 2013.

[31] Y. N. Ovchinnikov and I. M. Sigal. Ginzburg-Landau equation III. Vortex dynamics. *Nonlinearity*, 11(5):1277–1294, 1998.

[32] D. Pelinovsky and Y. Stepanyants. New multisoliton solutions of the Kadomtsev-Petviashvili equations. *Pis'ma Zh. Eksp. Teor Fiz*, 57(1):25–29, 1993.

[33] R. Penrose. Asymptotic properties of fields and space-times. *Phys. Rev. Lett.*, 10:66–68, 1963.

[34] L. Pismen. *Vortices in Nonlinear Fields: From Liquid Crystals to Superfluids, From Non-Equilibrium Patterns to Cosmic Strings*. International Series of Monographs on Physics (Book 100). Oxford University Press, 1999.

[35] D. Proment, M. Onorato, and C. F. Barenghi. Vortex knots in a Bose-Einstein condensate. *Phys. Rev. E*, 85:036306, 2012.

[36] Python Software Foundation. *Python Language Reference, version 2.7*.

[37] P. Roberts and N. Berloff. *Nonlinear Schrödinger equation as a model of superfluid helium*, volume 571 of *Lecture Notes in Physics*. Springer-Verlag, Providence, RI, 2001.

[38] Scilab Enterprises. *Scilab: Le logiciel open source gratuit de calcul numérique*. Scilab Enterprises, Orsay, France.

[39] J. Villarroel and M. J. Ablowitz. On the discrete spectrum of the nonstationary Schrödinger equation and multipole lumps of the Kadomtsev-Petviashvili I equation. *Comm. Math. Phys.*, 207(1):1–42, 1999.

[40] Z.-Q. Wang and M. Willem. A multiplicity result for the generalized Kadomtsev-Petviashvili equation. *Topol. Methods Nonlinear Anal.*, 7(2):261–270, 1996.

[41] M. I. Weinstein. On the vortex solutions of some nonlinear scalar field equations. *Rocky Mountain J. Math.*, 21(2):821–827, 1991. Current directions in nonlinear partial differential equations (Provo, UT, 1987).